



Available online at www.sciencedirect.com

jmr&t
Journal of Materials Research and Technology

journal homepage: www.elsevier.com/locate/jmrt



Letter

Dynamic recrystallization behavior of low-carbon steel during hot rolling process: modeling and simulation



ABSTRACT

Keywords:

Bar rolling
Dynamic recrystallization
Hot deformation
Numerical simulation
Physical simulation

DRX (dynamic recrystallization) behavior, which can improve the product's microstructure and enhance its performance, is vital in the high-temperature plastic deformation of metal materials. In this paper, single-pass hot compression tests were carried out on a Gleeble-3800 thermo-mechanical simulator to investigate the DRX behavior of a low carbon steel at a deformation temperature of 900 °C–1100 °C and a strain rate of 0.01 s^{−1}–0.1 s^{−1}. The effect of temperature and strain rate on DRX was investigated based on the direct connection between DRX and dynamic softening behavior. The Zener–Hollomon model revealed the relationship between temperature, strain rate, and stress was established. A DRX kinetic model was established for the hot-rolled condition based on the relationship between the characteristic parameters of DRX and temperature and strain rate. The results showed that the predicted and tested values were in good agreement. The established DRX kinetic model was embedded into DEFORM-3D software to simulate the DRX behavior of the hot rolling process of a round bar. The results showed that the fraction of DRX of the whole section of the bar after hot rolling showed noticeable non-uniformity. The DRX ability of the surface area in direct contact with the roller is significantly lower than in other areas. This phenomenon is related to the high-temperature deformation behavior during the rolling process. Reducing the roller speed has almost no effect on this phenomenon; increasing the rolling temperature can significantly improve this phenomenon.

..

1. Introduction

The hot rolling process is an essential form of bar production due to its high efficiency and automation [1,2]. During the hot rolling process, the material undergoes a complex high-temperature deformation behavior consisting of shape change and microstructure evolution [3–6]. As an essential part of the microstructure evolution, DRX behavior refines the coarse austenite grains and, through stress softening phenomenon, affects the shape change process, determining production's mechanical properties and shapes [7–10]. Therefore, DRX behavior attracts continuous and extensive attention from domestic and international researchers. Zhu et al. investigated the DRX behavior of Cr–Ni–Mo–Nb steel at deformation temperatures of 950 °C–1150 °C and strain rates

of 0.1 s^{−1}–5 s^{−1} by hot compression tests, the results showed that the DRX behavior is very sensitive to temperature and DRX hardly occurs at 950 °C [11]. Han et al. investigated the DRX behavior of 0.58C–1.89Mn–1.57Si–0.88Cr bainite steel at deformation temperatures of 950 °C–1150 °C and strain rates of 0.005 s^{−1}–5 s^{−1} by hot compression tests. DRX kinetic model was established to quantitatively describe the relationships between the fraction of DRX and deformation conditions. Furthermore, the microstructure was investigated under different deformation conditions. The results showed that high temperature and low strain rates could promote DRX behavior [12]. Kumar et al. investigated the DRX behavior of nickel-based alloys at different strain rates by hot compression tests combined with EBSD tests. The results show that the strain rate has a complex effect on the DRX behavior due to the adiabatic temperature rise [13]. The above research

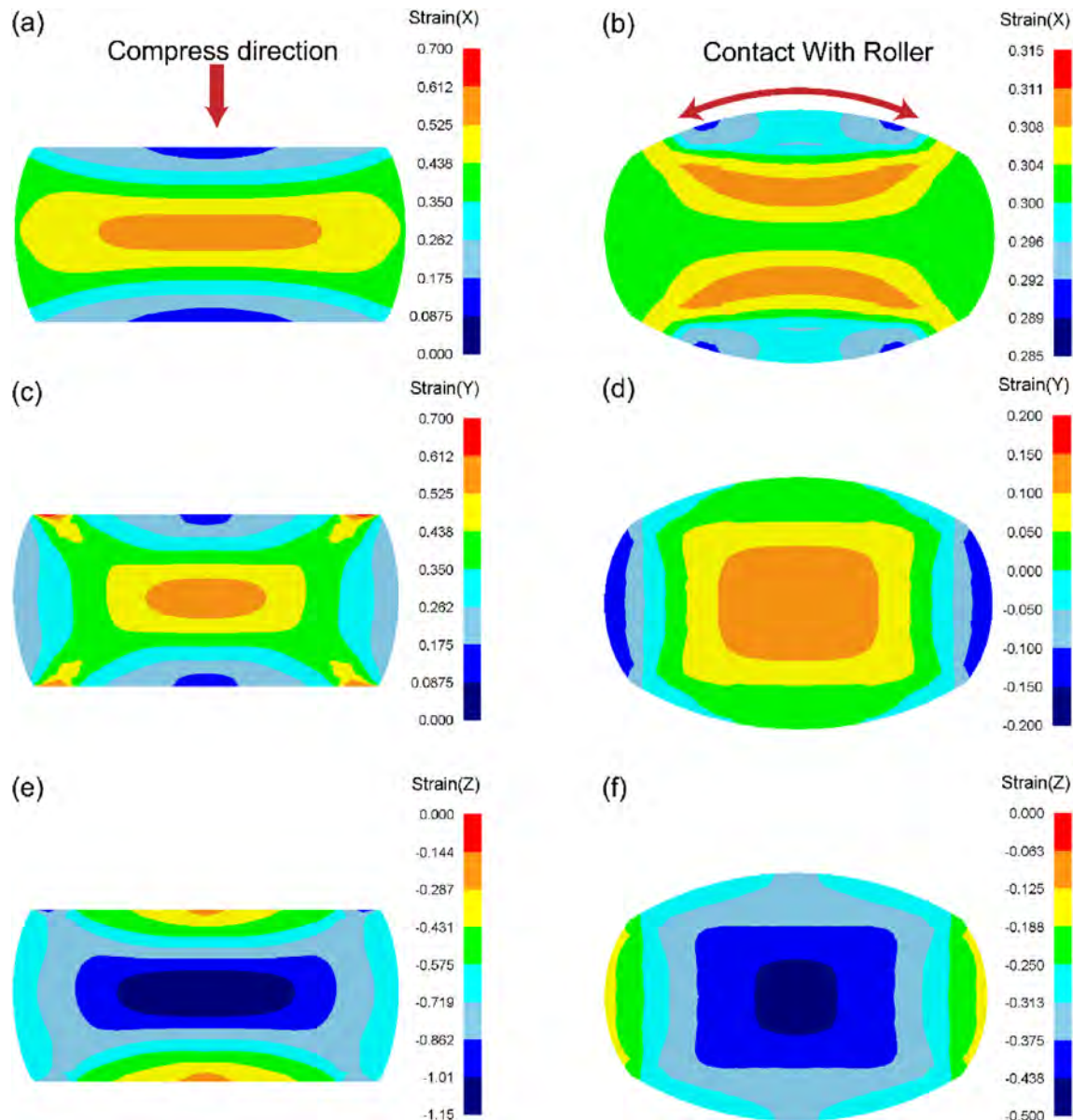


Fig. 1 – Strain State (a) in X direction during compression, (b) in X direction during bar rolling, (c) in Y direction during compression, (d) in Y direction during bar rolling, (e) in Z direction during compression, (f) in Z direction during bar rolling.

illustrates that the deformation conditions (strain, strain rate, deformation temperature) greatly influence DRX behavior. During hot rolling, different deformation regions experience different deformation processes [14–16]. Therefore, the DRX kinetic model is usually incorporated into finite element software to investigate the DRX behavior in the hot rolling process. Ding et al. investigated the effect of rolling process parameters on DRX behavior during hot strip rolling by DEFORM-3D. The results showed that the development of rolling temperature on DRX behavior was more drastic than roller speed. The strip obtained ideal microstructure through DRX behavior at high roller speed and rolling temperature [17]. Gu et al. studied the microstructure evolution of GCr15 steel rod during hot rolling by a commercial finite element software MSC. Marc. The dynamic recrystallization behavior and grain size evolution under the hot rolling process were accurately

predicted. Still, the coupling relationship between rolling process parameters and DRX behavior was not discussed in detail [18]. Wang et al. investigated the DRX behavior during single-pass hot rolling of bars in a round-oval roller system by Abaqus software. The results showed that rolling temperature dramatically affects the fraction of DRX. Increasing rolling temperature could significantly increase the fraction of DRX after rolling [19]. Based on the previous research mentioned above, many investigations have been focused on DRX

Table 1 – Chemical composition of the experimental steel.

C	Si	Cr	Mn	P	S	Cu	Al	Fe
0.121	0.063	0.007	0.104	0.023	0.256	0.039	0.097	99.29

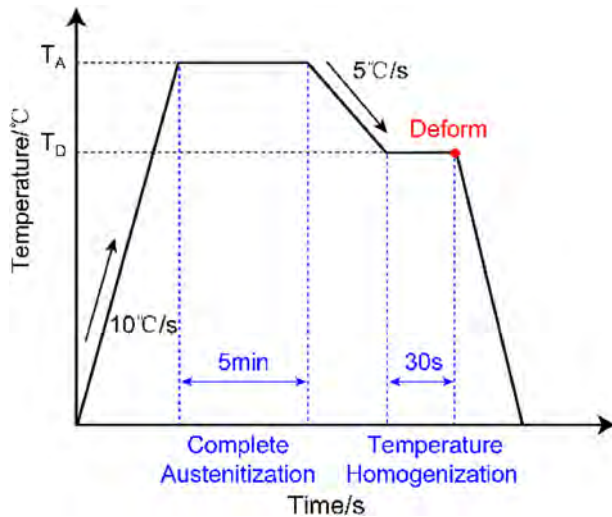


Fig. 2 – The test procedure.

behavior in recent years. However, there are still two deficiencies: 1) Currently, the DRX kinetic model was established based on the stress softening behavior at a fixed strain rate. However, the deformation conditions significantly affect the DRX behavior, which leads to the previous method's lack of persuasiveness. 2) Due to different deformation conditions, bar rolling exhibits significant non-uniformity in the fraction of DRX over the entire cross-section, affecting the mechanical properties of the bar. The present research lacks a specific explanation of the causes of this phenomenon and how it behaves under different rolling process parameters. Therefore, in this study, the bar rolling process is physically stimulated by hot compression tests to establish a DRX kinetic model applicable in different deformation conditions. The DRX kinetic model was incorporated into finite element software to simulate the hot rolling process of bars. Reasons for the non-uniformity of the fraction of DRX and its performance under different rolling process parameters were analyzed.

2. Experimental procedures

In order to establish a physical model describing the deformation behavior of materials at high temperature, physical simulation tests such as thermal compression (cylindrical compression test [20] and plane strain test [21]), tensile [17], and torsion [22] are widely used to obtain a relationship between deformation conditions and flow stress. Among the above experiments, the constitutive model under the cylindrical hot compression test is widely used to describe the hot rolling behavior of bars. Different scholars have verified it from the aspects of shape change [23], rolling force [14], and recrystallization behavior [18,19,24,25]. This consistency may be attributed to the approximate strain state of cylindrical specimen compression and bar rolling. Fig. 1(a), (c), and (e) show the strain state of the central section after deformation in the X, Y, and Z directions of the cylindrical specimen. During the compression process, the cylindrical sample undergoes height reduction and radial expansion. The core will

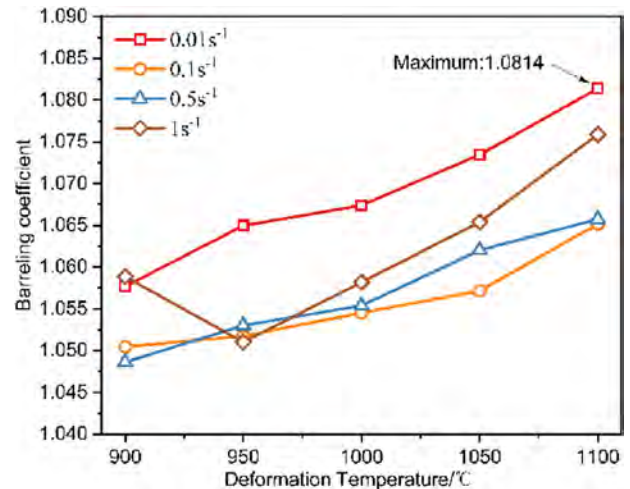


Fig. 3 – Bulging coefficient under different conditions.

bear more significant deformation because it is not limited by friction with the anvil. Moreover, it is in tension in the X and Y directions and compression in the Z direction. Fig. 1(b), (d), and (f) show the strain state of the central section after deformation in three directions of X, Y, and Z during bar rolling. During the rolling process, the bar will extend in the X direction (rolling direction), expand in the Y direction, and compress in the Z direction. The surface extension in the X direction is slightly less than the core due to the friction surface with the roller. The core is in tension in the Y direction, and the sides that are not in direct contact with the rolls are compressed. This strain state is caused by friction between the bar and the roll and passes restrictions during the spreading process. In the Z direction, the entire bar is compressed and deformed, and the deformation of the side surface is the smallest because it is not in direct contact with the roller. Bar rolling and cylindrical compression generally produce close deformations in the core region. Therefore, in this paper, the compression of cylindrical specimens is used to describe the high-temperature deformation behavior of hot bar rolling.

The experimental material was taken from a hot-rolled low carbon steel strip. Table 1 presents the chemical composition in mass%. The single-pass hot compression tests were performed on a Gleeble-3800 thermo-mechanical simulator. The $\phi 10 \times 15$ mm cylindrical specimens used for the hot compression tests are machined from a hot-rolled strip by wire cutting.

It is worth noting that specimens need to be carefully ground and polished before the tests, ensuring surface smoothness. Two K-type thermocouples are welded to the longitudinal center of the cylindrical specimen and connected directly to the Gleeble-3800 thermo-mechanical simulator for the automatic temperature measurement. Square tantalum sheets molybdenum disulfide high-temperature lubricant is applied between the anvil and the specimen to reduce friction and avoid adhesion during deformation. Before the test, the air in the chamber is extracted to form a vacuum and filled with argon gas. Moreover, the chamber door joints need to be sealed with silicone grease to reduce oxidation. During the

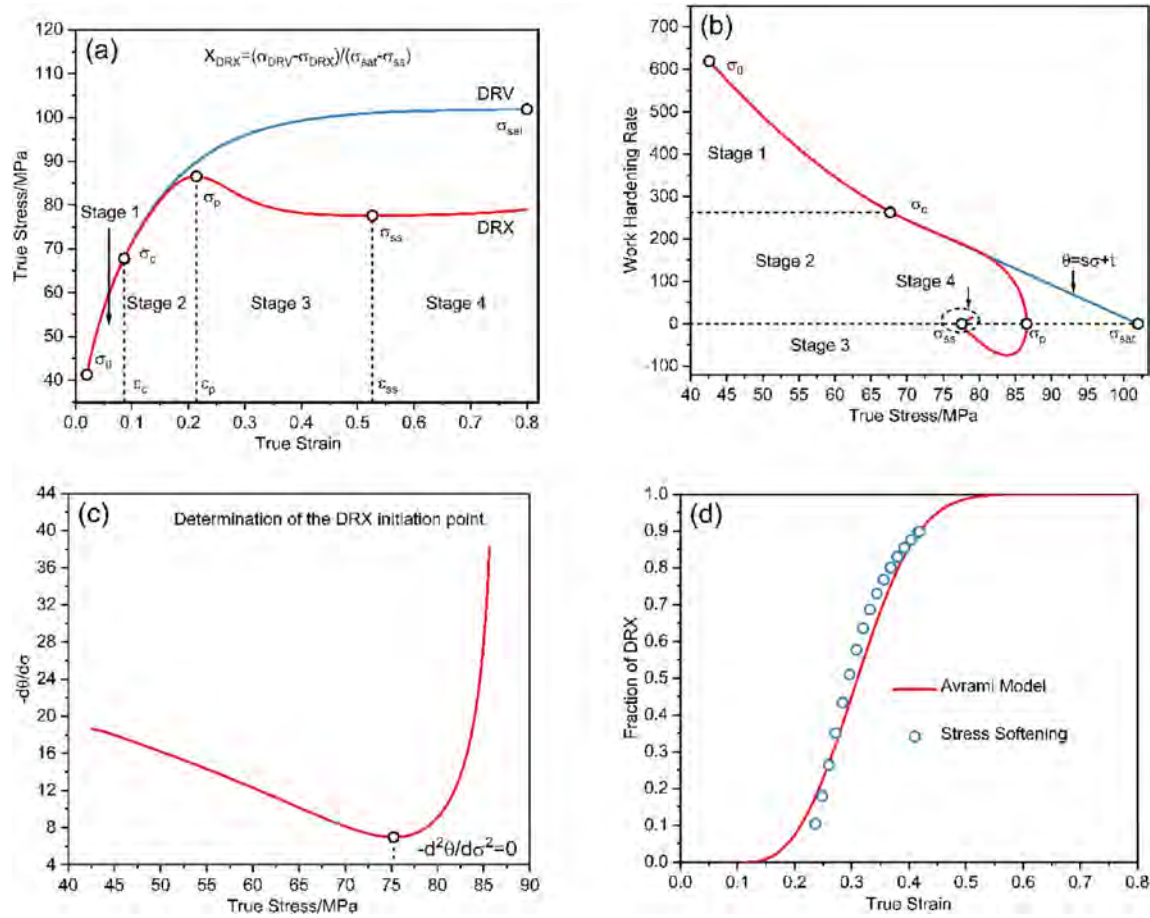


Fig. 4 – Schematic diagram of (a) different types of flow stress curves, (b) DRX typical work hardening rate curve, (c) DRX critical point determination process, (d) Avrami DRX kinetic model fitting process.

test, the specimen is first heated to 1150 °C at a heating rate of 10 °C/s and held for 5min for fully austenitizing. Then the temperature furthermore is cooled to the deformation temperature (900 °C, 950 °C, 1000 °C, 1050 °C, 1100 °C) at a rate of 5 °C/s and held for 30 s to obtain a uniform temperature distribution. The temperature accuracy is guaranteed by K-type thermocouples welded to the specimen. Subsequently, the samples were deformed to a true strain of 0.8 (60%) at a strain rate of 0.01 s⁻¹, 0.1 s⁻¹, 0.5 s⁻¹, and 1 s⁻¹. The true stress–strain data will be recorded by the Gleeble-3800 thermo-mechanical simulator. Twenty specimens were subjected to the hot compression tests. The test procedure is shown in Fig. 2.

3. Result and discussion

3.1. DRX behavior analysis

3.1.1. True stress–strain curve analysis

The accuracy of flow stress data is the prerequisite for accurately describing the high-temperature deformation behavior of materials. Although the experimental research has tried to

avoid the influence of friction, the bulging phenomenon of cylindrical samples is still inevitable. The bulging influence coefficient B (Eq. (1)) is used to describe the influence of friction and evaluate the necessity of correcting the friction influence [26]:

$$B = \frac{hR_M^2}{h_0R_0^2} \quad (1)$$

where h , R_M , h_0 and R_0 are the height of the sample after deformation, the maximum radius, the initial height, and the initial radius. When the bulging influence coefficient B is greater than or equal to 1.1, it is necessary to correct the frictional influence of the stress–strain curve. The B value under different deformation conditions is shown in Fig. 3, and the bulging phenomenon becomes more evident with the increase in temperature. In the case of high temperatures, the center is more likely to be deformed, which aggravates the uneven deformation. This is also consistent with the subsequent uneven deformation of the bar. The strain rate has no pronounced effect on the bulging phenomenon, which may be related to the adiabatic heating phenomenon caused by the increase of the strain rate. The maximum value of the bulging influence coefficient B is 1.0814, which appears at 0.01 s⁻¹ and 1100 °C deformation conditions, and is less than the necessary correction value (1.1). However, in order to accurately describe

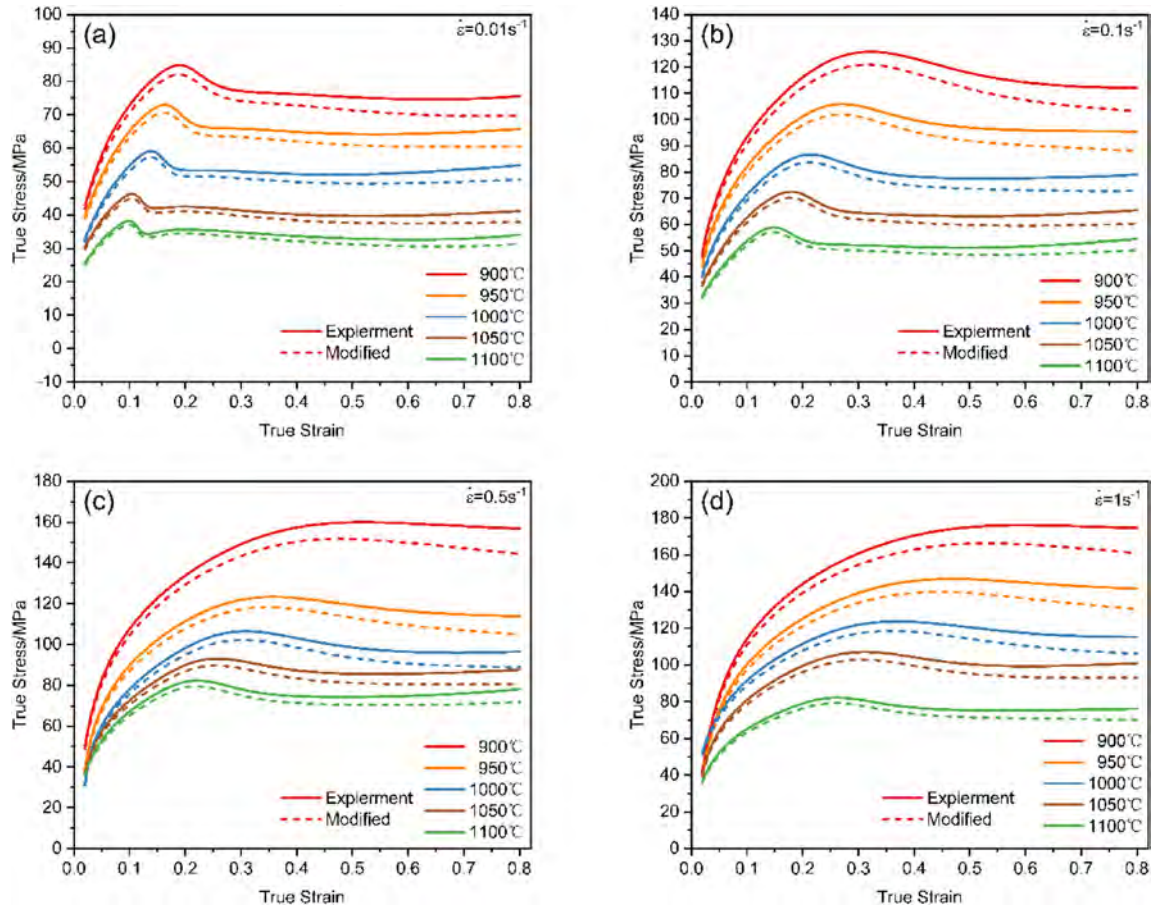


Fig. 5 – Flow stress curves at different strain rates (a) 0.01 s^{-1} , (b) 0.1 s^{-1} , (c) 0.5 s^{-1} , (d) 1 s^{-1} .

the high-temperature deformation behavior of materials, Eq. (2) [27,28] is used to correct the flow stress, and the results are shown in Fig. 5:

$$\bar{\sigma} = \frac{\sigma}{1 + \left(\frac{2}{3\sqrt{3}}\right)m\left(\frac{r_0}{h_0}\right)\exp\left(\frac{3\varepsilon}{2}\right)} \quad (2)$$

where $\bar{\sigma}$, σ , m , r_0 , h_0 , and ε are the corrected flow stress, the test flow stress, the friction coefficient, the initial radius of the specimen, the initial height of the specimen, and the test strain, respectively.

DRX behavior during high-temperature deformation of materials is directly related to the stress softening phenomenon [7,29,30]. As shown in Fig. 4(a), the work hardening and DRX and DRV reached an equilibrium under different softening mechanisms during the deformation process. When the primary softening mechanism is DRV, the stress has no apparent downward trend and reaches the maximum value (saturation stress σ_{sat}) under dynamic recovery as the deformation progresses. The stress exhibits an evident softening phenomenon when the primary softening mechanism is DRX. The stress reaches the maximum value (peak stress σ_p), rapidly decreases to the steady-state stress σ_{ss} , and maintains equilibrium during the subsequent deformation. The description of this hardening-

softening mechanism concerning material flow stress has been extensively studied, demonstrated, and applied [6,19,31].

The flow stress curves at different deformation conditions are shown in Fig. 5. In the deformation temperature range of 900°C – 1100°C and strain rate of 0.01 s^{-1} – 1 s^{-1} , most of the flow stress curves exhibit significant DRX softening behavior, indicating the occurrence of DRX behavior, except for a few low temperature, high strain rate deformation conditions (0.5 s^{-1} , 1 s^{-1} at 900°C). It is worth noting that part of the end of the flow stress curve appears upturned, which is caused by the increase in friction as the contact area between the sample and the anvil increases. Fig. 6(a) shows the flow stress curves and the corresponding peak stress σ_p in different deformation temperatures at 0.5 s^{-1} . As the deformation temperature decreases, the peak stress and the required strain (peak strain ε_p) increase significantly, and the softening effect of DRX decreases. The flow stress–strain curve at 900°C showed almost no softening behavior, indicating that low temperature suppressed the DRX behavior. Fig. 6(b) shows the flow stress–strain curves and the corresponding peak stress σ_p at different strain rates at 900°C . As the strain rate increases, the DRX softening behavior significantly weakens, indicating that the increase in strain rate weakens the material's DRX ability.

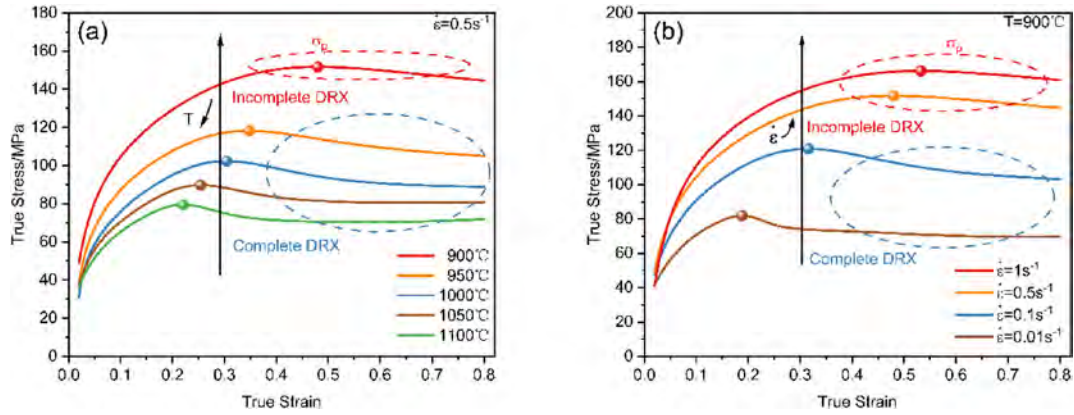


Fig. 6 – Flow stress curves and corresponding peak stress σ_p (a) at 900 °C, 950 °C, 1000 °C, 1050 °C, 1100 °C under 0.5 s⁻¹, (b) at 900 °C under 0.01 s⁻¹, 0.1 s⁻¹, 0.5 s⁻¹, 1 s⁻¹.

The mechanism of DRX behavior can illustrate these phenomena. The temperature drops, weakening the thermal activation of the atoms. The ability to form new grains through DRX behavior is weakened, which slows down the dislocations elimination, resulting in a weaker softening effect. The strain rate increases result in reduced deformation time. New grains have insufficient time to form by DRX behavior, which inhibits the softening effect.

3.1.2. Critical strain

During high-temperature deformation, the DRX behavior is activated only when the dislocation density reaches a critical value (critical strain ϵ_c) [7,29,32,33]. To determine whether DRX behavior occurs, it is essential to find the critical strain and quantitatively characterize the relationship between critical strain and deformation conditions to establish the DRX kinetic model. In this paper the method proposed by

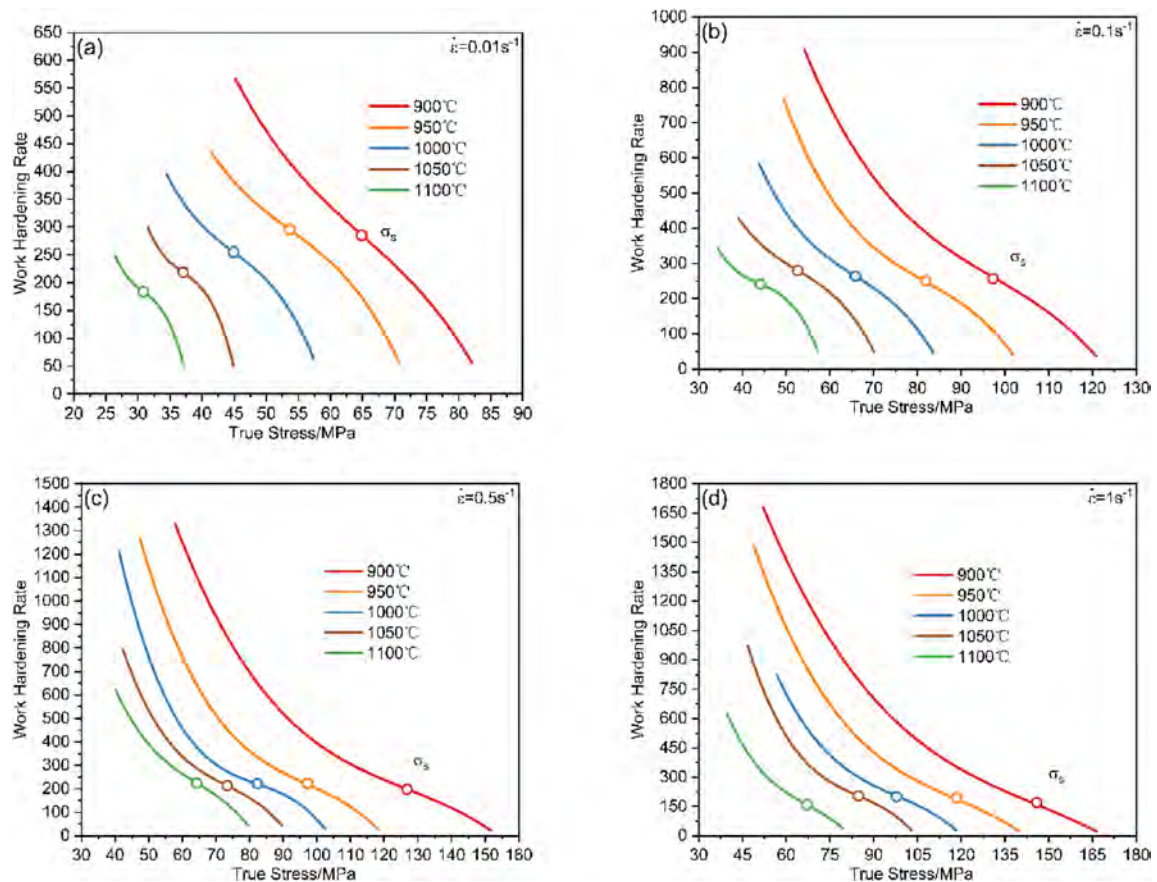


Fig. 7 – Work hardening rate curves at different strain rates (a) 0.01 s⁻¹, (b) 0.1 s⁻¹, (c) 0.5 s⁻¹, (d) 1 s⁻¹.

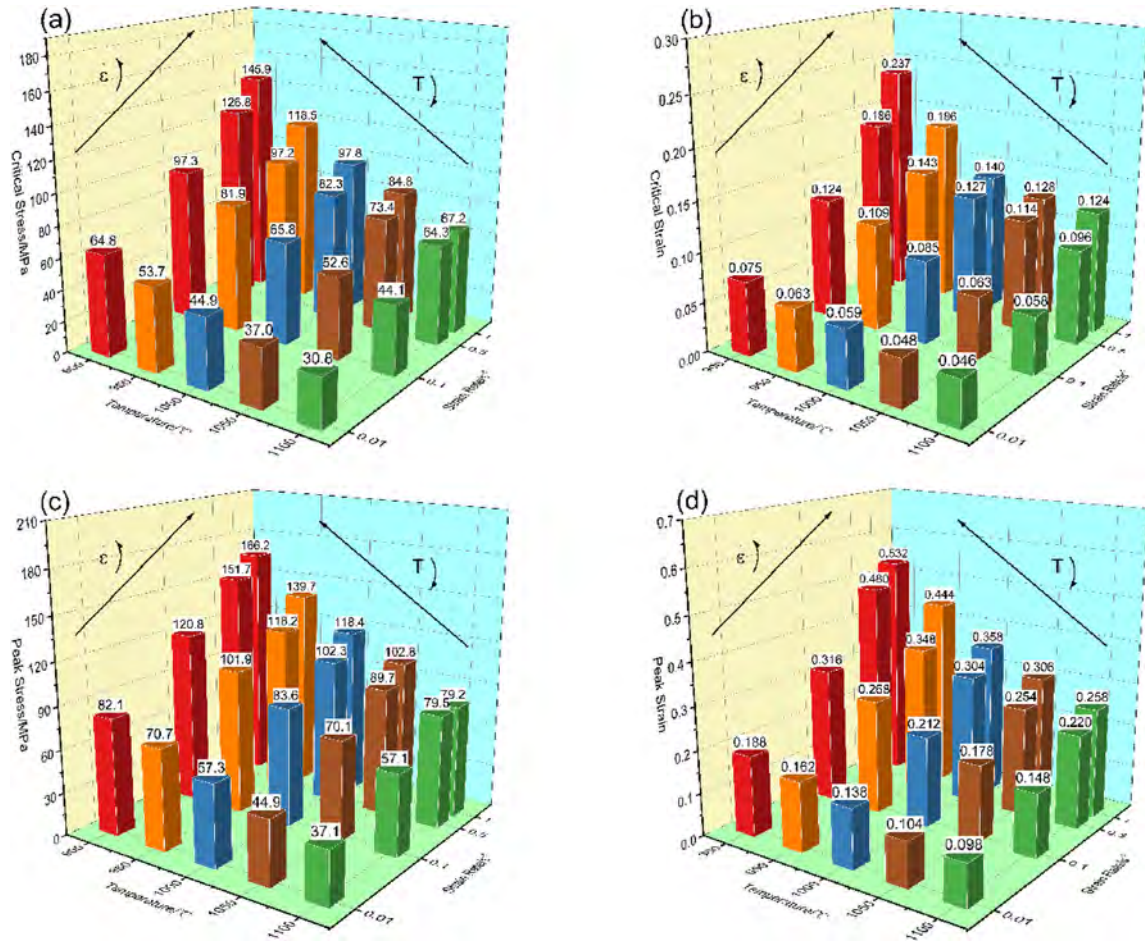


Fig. 8 – Characteristic parameters of DRX under different deformation conditions (a) critical stress σ_c , (b) critical strain ϵ_c , (c) peak stress σ_p , (d) peak strain ϵ_p .

Najafizadeh and Jonas [34,35] to determine the critical value of DRX behavior was used. As shown in Fig. 4(b), in the initial deformation stage, the work hardening rate decreases continuously at a gradually slowing rate, which is caused by the combined effects of work hardening and dynamic recovery softening. As the deformation progresses, DRX behavior occurs, many dislocations are eliminated, the rate of decrease in the work hardening rate increases rapidly, and the work hardening rate curve appears at an inflection point. As the DRX behavior further occurs, the work hardening rate drops rapidly to 0 point, and the stress reaches a maximum value (peak stress σ_p). Eventually, the work-hardening rate stabilizes around 0 under the combined action of DRX behavior and work-hardening, and the flow stress reaches a steady-state (steady-state stress σ_{ss}) [32,34]. Therefore, the work hardening rate before peak stress ($\theta = \frac{\partial \sigma}{\partial \epsilon}$) is fitted with a cubic polynomial to the stress, and the inflection point of the curve determines the DRX critical point ($\frac{\partial^2 \theta}{\partial \sigma^2} = 0$), which is shown in Fig. 4(c). The work hardening rate curves and critical points under different deformation conditions are shown in Fig. 7.

Fig. 8 shows the critical stress σ_c , critical strain ϵ_c , peak stress σ_p , and peak strain ϵ_p under different deformation conditions. With increasing strain rate and decreasing

deformation temperature, the critical stress σ_c , critical strain ϵ_c , peak stress σ_p , and peak strain ϵ_p increase to a similar degree. The results reaffirm that high strain rates

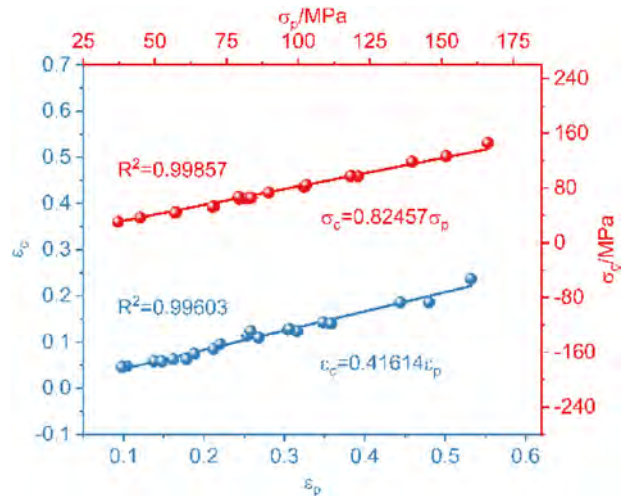


Fig. 9 – Linear relationship between critical stress σ_c and peak stress σ_p , critical strain ϵ_c and peak strain ϵ_p .

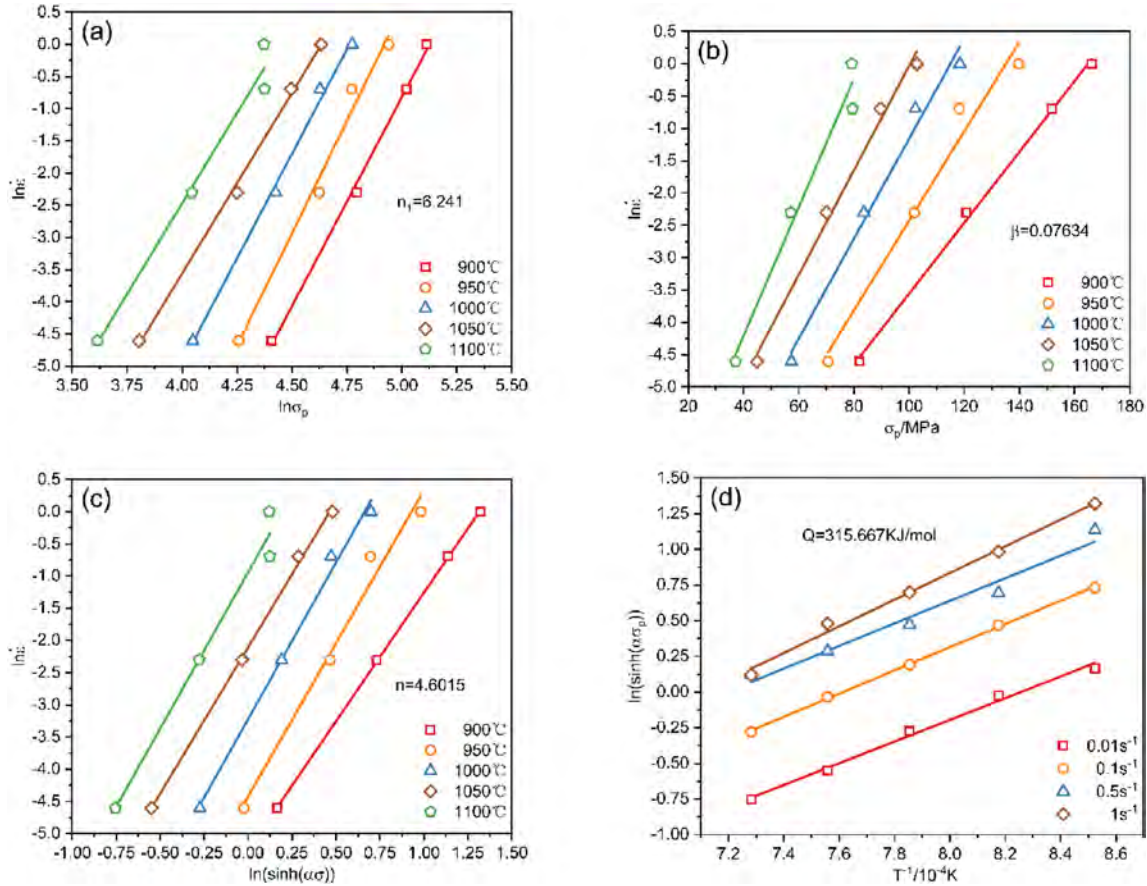


Fig. 10 – Material constants and activation energy of deformation calculation (a) $\ln \dot{\epsilon} - \sigma_p$, (b) $\ln \dot{\epsilon} - \ln \sigma_p$, (c) $\ln \dot{\epsilon} - \ln[\sin(\alpha \sigma_p)]$, (d) $\ln[\sin(\alpha \sigma_p)] - T^{-1}$.

and low deformation temperatures suppress the occurrence of DRX behavior in one aspect. On the other hand, it also shows a relationship between critical stress and peak stress and between critical strain and peak strain. The results of linear fitting of critical stress and peak stress, critical strain, and peak strain are shown in Fig. 9. A good linear relationship can be seen between them: $\sigma_c = 0.82457\sigma_p$, $\epsilon_c = 0.41614\epsilon_p$.

3.1.3. Zener–Hollomon model

The above discussion shows a significant relationship between DRX behavior characteristic parameters, temperature and strain rate. To quantitatively characterize this relationship, the Zener–Hollomon model, coupling the interaction between deformation temperature, strain rate, and stress, is widely used [36–42], which can be demonstrated as:

$$Z = \dot{\epsilon} \exp\left(\frac{Q}{RT}\right) = A[\sin(\alpha \sigma)]^n \quad (3)$$

where σ is the flow stress is usually chosen for the calculation, Q is the heat deformation activation energy, R is the gas constant ($8.314 \text{ J} \cdot \text{mol}^{-1} \cdot \text{K}^{-1}$), T is the absolute temperature, A , α , n are materials constants. To solve the deformation activation energy Q and materials constants A , α , n , the Arrhenius equation, describing the relationship

between flow stress, strain rate, and deformation temperature during high-temperature deformation, is widely used [43–47].

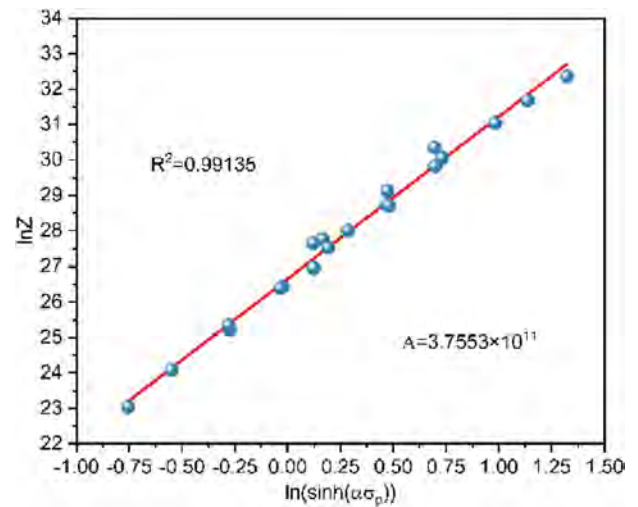


Fig. 11 – Relationship between peak stress σ_p and Zener–Hollomon parameters.

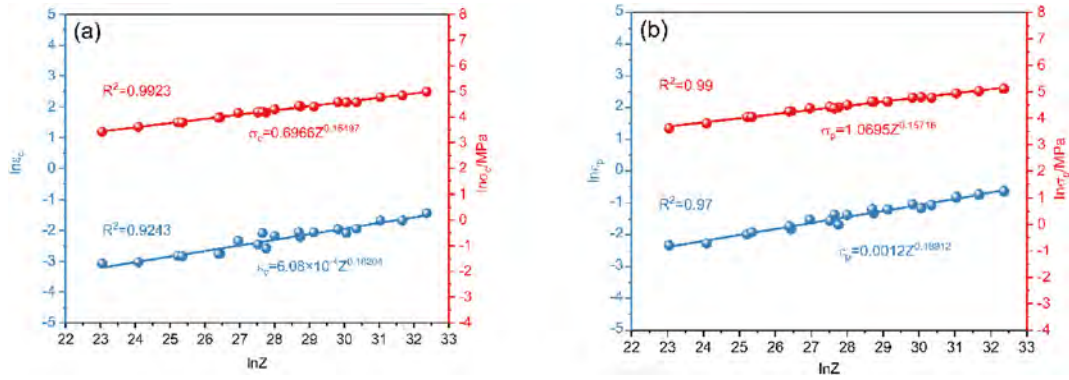


Fig. 12 – Relationship between Zener–Hollomon model and DRX characteristic parameters (a) critical stress σ_c , critical strain ϵ_c , (b) peak stress σ_p , peak strain ϵ_p .

$$\dot{\epsilon} = \begin{cases} A_1 \sigma^{n_1} \exp\left(-\frac{Q}{RT}\right) (\alpha \sigma < 0.8) \\ A_2 \exp(\beta \sigma) \exp\left(-\frac{Q}{RT}\right) (\alpha \sigma \geq 1.2) \\ A[\sin(\alpha \sigma)]^n \exp\left(-\frac{Q}{RT}\right) (\text{all conditions}) \end{cases} \quad (4)$$

where A_1 , A_2 , n_1 , β are materials constants, and $\alpha \approx \beta/n_1$.

To calculate these parameters, a logarithmic transformation of Eq. (5) is required.

$$\ln \dot{\epsilon} = \begin{cases} n_1 \ln \sigma + \ln A_1 - Q/RT (\alpha \sigma < 0.8) \\ \beta \sigma + \ln A_2 - Q/RT (\alpha \sigma \geq 1.2) \\ n \ln[\sin(\alpha \sigma)] + \ln A - Q/RT (\text{all conditions}) \end{cases} \quad (5)$$

To obtain α , β and n_1 should be calculated first. From Eq. (5), it can be seen $\beta = \frac{\partial \ln \dot{\epsilon}}{\partial \sigma}$ and $n_1 = \frac{\partial \ln \dot{\epsilon}}{\partial \ln \sigma}$. By linearly fit $\ln \dot{\epsilon}$ and σ_p , $\ln \dot{\epsilon}$ and $\ln \sigma_p$ at different temperatures, β and n_1 can be obtained as 0.07634 and 6.541. And α can be calculated as 0.0122.

To calculate the activation energy of deformation Q and the material constant n , Eq. (6) should be transformed as:

$$Q = Rn \frac{\partial \ln[\sin(\alpha \sigma)]}{\partial 1/T} \quad (6)$$

$$n = \frac{\partial \ln \dot{\epsilon}}{\partial \ln[\sin(\alpha \sigma)]} \quad (7)$$

By linear fitting $\ln \dot{\epsilon}$ and $\ln[\sin(\alpha \sigma_p)]$ at different deformation temperatures, n can be obtained as 4.6015. A linear fit of $\ln[\sin(\alpha \sigma_p)]$ and $1/T$ at different strain rates was performed to find the average slope value. And the activation energy of deformation Q can be obtained as $315 \text{ KJ} \cdot \text{mol}^{-1}$.

Take the logarithm of both sides of Eq. (3) to obtain the following equation:

$$\ln Z = n \ln[\sin(\alpha \sigma_p)] + \ln A \quad (8)$$

By linear fitting of $\ln Z$ and $\ln[\sin(\alpha \sigma_p)]$ the linear intercept value which is $\ln A$ can be obtained, and $A = 3.7553 \times 10^{11}$.

Now the Zener–Hollomon model can be obtained as:

$$Z = \dot{\epsilon} \exp\left(\frac{315667}{RT}\right) = 3.7553 \times 10^{11} [\sinh(0.0122 \sigma_p)]^{4.6015} \quad (9)$$

The fitting process is shown in Figs. 10 and 11.

Previous studies showed that based on the Zener–Hollomon model, the relationship between the DRX characteristic parameters (critical stress σ_c , critical strain ϵ_c , peak stress σ_p , and peak strain ϵ_p) strain rate, and deformation temperature can be established by the following equation [7,19,30]:

$$p = kZ^n \quad (10)$$

where p is the DRX characteristic parameter, k and n are the materials constants. The corresponding relationship between Z and DRX characteristic parameters is shown in Fig. 12. The relationship can be expressed as: $\sigma_c = 0.6966Z^{0.16497}$, $\epsilon_c = 6.08 \times 10^{-4} Z^{0.18204}$, $\sigma_p = 1.0695Z^{0.15716}$, $\epsilon_p = 0.0012Z^{0.18912}$.

The coupling relationship among activation energy of deformation Q , Zener–Hollomon factor, and DRX characteristic parameters has received extensive attention in studying material thermal processing behavior. It is important to evaluate high-temperature deformation behavior and measure DRX capability. Fig. 13(a) compares the activation energy of deformation of different low carbon steel (LC) [48–54], medium carbon steel (MC) [11,12,30,43,54–58], stainless steel (SS) [9,20,36,44,59–63]. The activation energy of deformation is directly related to the deformation mechanism and capability. As the activation energy of deformation increases, the material deformation mechanism changes from diffusion, DRV to DRX. The activation energy of deformation of low carbon steel is generally between 280 and 370 KJ/mol, which is higher than the activation energy of γ iron self-diffusion. This is attributed to the combined effect of element drag and particle precipitation after alloying element addition. The activation energy of deformation of medium carbon steel is slightly smaller than that of low carbon steel. This is attributed to the increase in the self-diffusion coefficient of iron atoms due to the increase in carbon content, increasing the rate of atomistic mechanisms controlled by iron self-diffusion [54]. In order to improve the corrosion resistance, strength, and other properties of the material, a large amount of alloying elements such as Cr and Ni are added to stainless steel. The activation energy of deformation of stainless steel is generally between 380 and 500 KJ/mol, which is higher than that of carbon steel. This paper's activation energy of deformation is 315.667 KJ/mol, close to that of general C–Mn steel and micro-alloyed steel, which can be explained by the material's content of

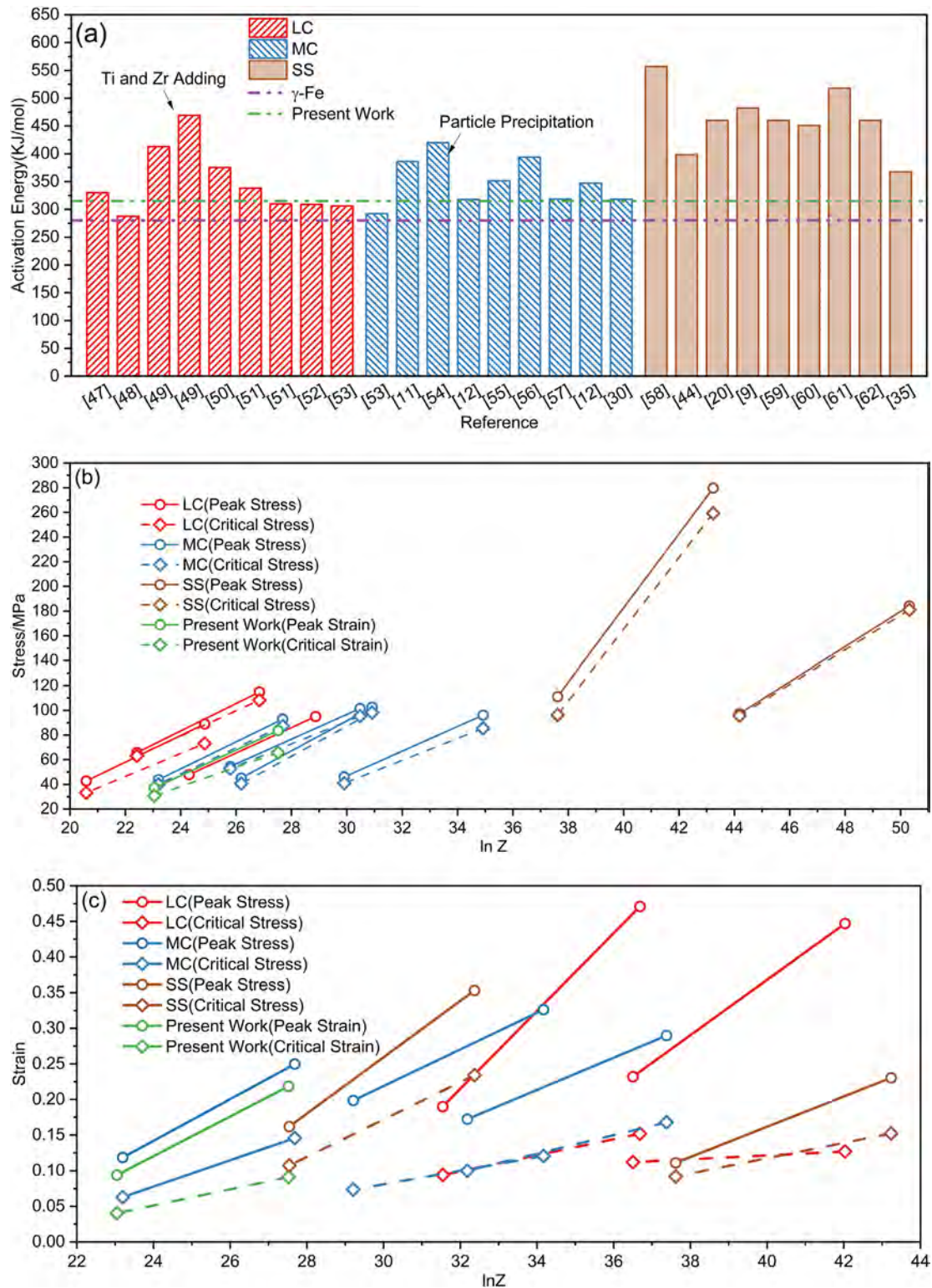


Fig. 13 – (a)Activation energy of deformation, (b) Relationship between DRX characteristic stress and Z, (c) Relationship between DRX characteristic strain and Z in low carbon steel, medium carbon steel and stainless steel.

alloying elements. Fig. 13(b) compares the characteristic stress of different low carbon steels [48,49,51], medium carbon steels [12,43,56–58], and stainless steels [9,44] and Z at the deformation condition of 1000 °C, 0.1s⁻¹ and 1100 °C, 0.01s⁻¹. The addition of alloying elements increases the activation energy

of deformation, resulting in an increase in Z under the same deformation conditions. However, it has little effect on the characteristic stress value of low and medium carbon steel. The peak stress and critical stress are generally between 30 and 120 MPa. The addition of trace alloying elements has little

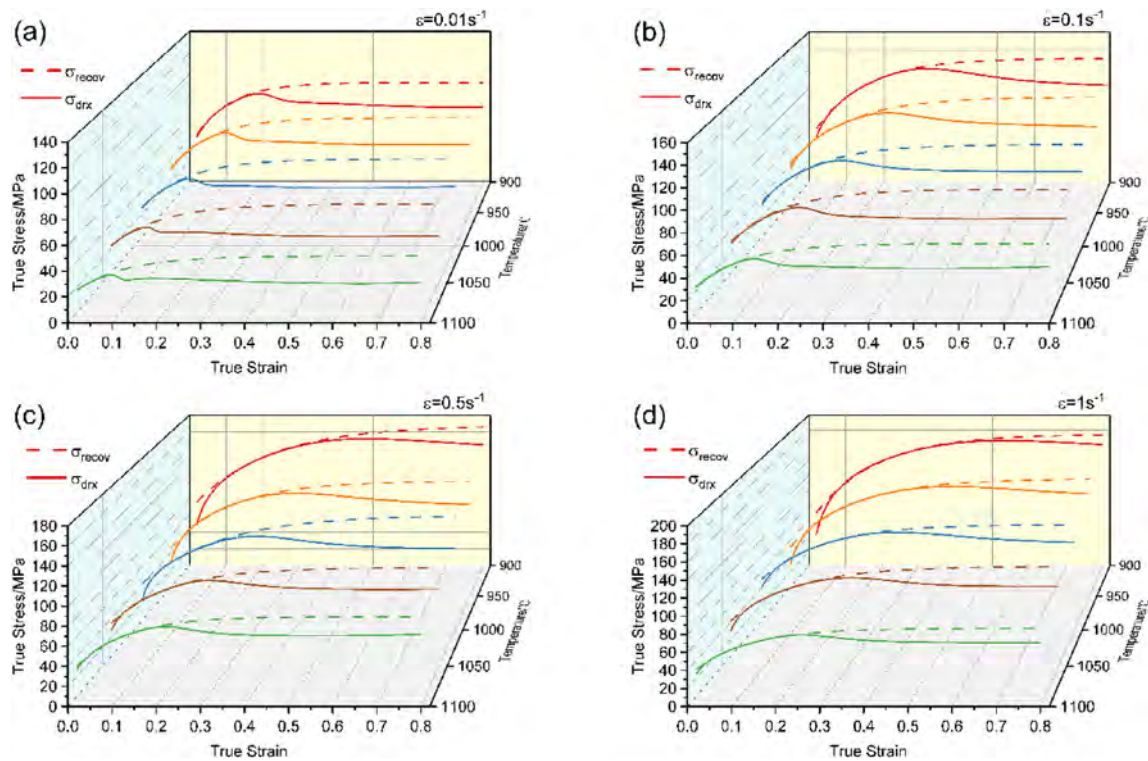


Fig. 14 – Comparison of dynamic recovery stress and DRX stress at different strain rates (a) 0.01 s^{-1} , (b) 0.1 s^{-1} , (c) 0.5 s^{-1} , (d) 1 s^{-1} .

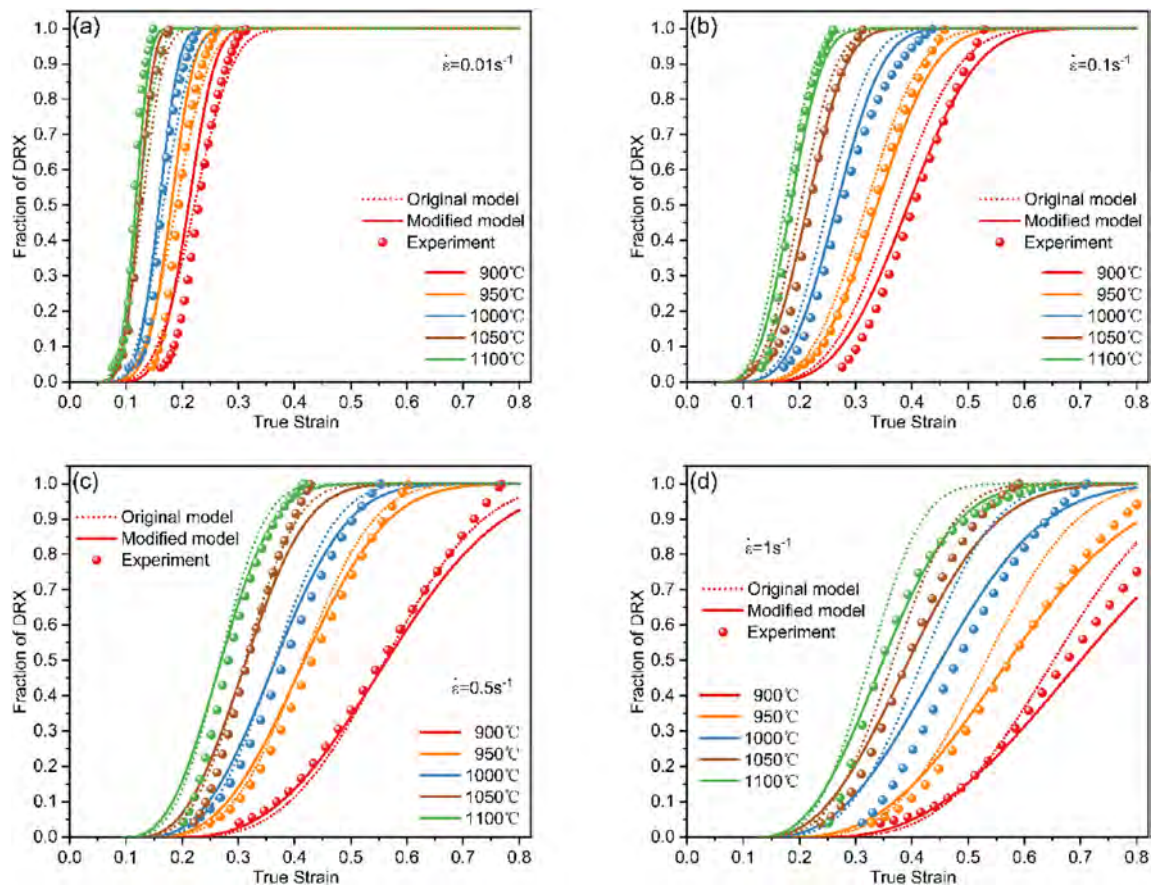


Fig. 15 – Comparison of predicted and experimental data of the fraction of DRX with different strain rates (a) 0.01 s^{-1} , (b) 0.1 s^{-1} , (c) 0.5 s^{-1} , (d) 1 s^{-1} .

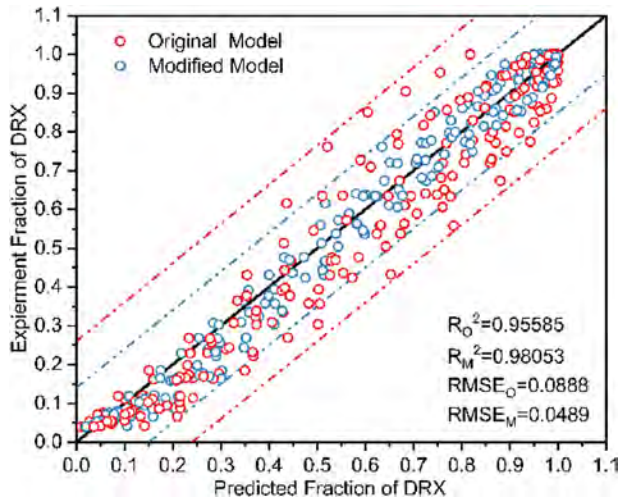


Fig. 16 – Comparison of the results of two DRX kinetic models.

effect on the deformation resistance of carbon steel. Many alloying elements such as Cr and Ni are added to stainless steel. On the one hand, increasing the activation energy of deformation leads to an increase in Z under the same deformation conditions. On the other hand, it significantly improves the deformation resistance, making it difficult for stainless steel to deform compared to carbon steel. The influence of material composition on DRX behavior is complex. For example, elements such as Cr and Mo have an inhibitory effect on DRX behavior [64]. The addition of the C element can reduce the critical strain of the material and promote the DRX behavior rate [49]. However, its effect is affected by the deformation temperature [65]. B element addition promotes DRX behavior [66,67]. N element addition provides more nucleation sites for DRX behavior, lowers the critical strain, and promotes DRX behavior [68]. Fig. 13(c) compares the relationship between characteristic strain of different low carbon steels [50], medium carbon steels [11,12,55], and stainless steels [9,36] and Z at deformation conditions of 1000 °C, 0.1s⁻¹ and 1100 °C, 0.01s⁻¹. The critical and peak

strain is lower in this paper, and DRX behavior is prone to occur.

3.1.4. DRX kinetic model

The stress softening phenomenon is the most direct effect of DRX behavior on high-temperature deformation behavior. Fig. 4(c) shows that the widely used method to establish DRX kinetic model is approximately replacing the fraction of DRX with the stress softening effect and fitting the stress softening effect according to Avrami DRX kinetic model [19,30,56,69,70].

The dynamic recovery stress should be calculated first to obtain the stress softening effect. Of the numerous methods to calculate the dynamic recovery stress, this paper uses the one proposed by Zahiri [71]. Based on the assumption that the work hardening rate decreases to zero in a nearly linear form when DRX does not occur, calculate the dynamic recovery stress by integrating the work hardening rate. As shown in Fig. 4(b), the blue line can be expressed as:

$$\theta = \frac{d\sigma}{d\varepsilon} = s\sigma + t \quad (\sigma_c \leq \sigma \leq \sigma_{sat}) \quad (11)$$

s and t are the slope and intercept of the straight line respectively, which can be expressed as:

$$s = \frac{\theta_c}{\sigma_{sat} - \sigma_c} \quad (12)$$

$$t = \frac{\theta_c \sigma_{sat}}{\sigma_{sat} - \sigma_c} \quad (13)$$

Eq. (11) can be transformed as:

$$s\sigma + t \frac{1}{d\sigma} = \frac{1}{d\varepsilon} \quad (14)$$

Therefore, the dynamic recovery stress can be calculated by integration:

$$\sigma_{DRV} = \frac{[(s\sigma_c + t)\exp(s\varepsilon - s\varepsilon_c) - t]}{s} \quad (15)$$

Fig. 14 shows the comparison of dynamic recovery stress and DRX stress at different deformation conditions.

Afterward, the stress softening effect is fitted to the strain under different deformation conditions according to the

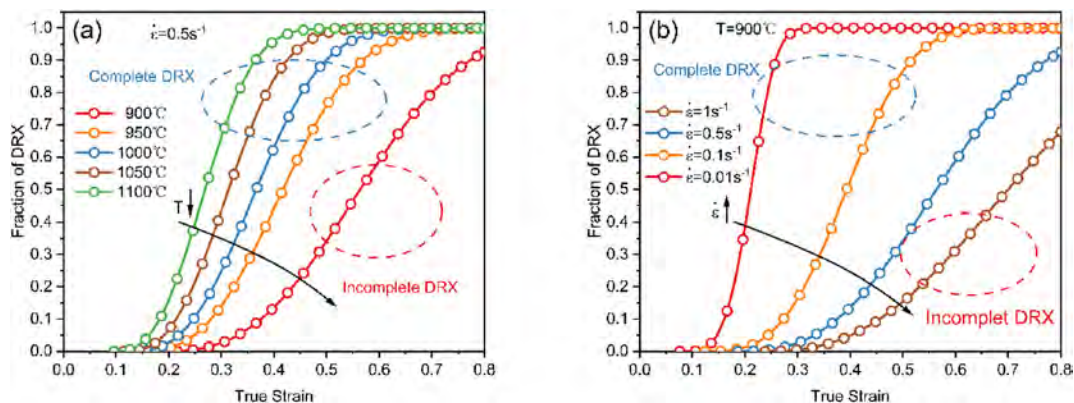


Fig. 17 – (a) the fraction of DRX curves at 900 °C, 950 °C, 1000 °C, 1050 °C, 1100 °C under 0.5 s⁻¹, (b) the fraction of DRX curves at 900 °C under 0.01 s⁻¹, 0.1 s⁻¹, 0.5 s⁻¹, 1 s⁻¹.

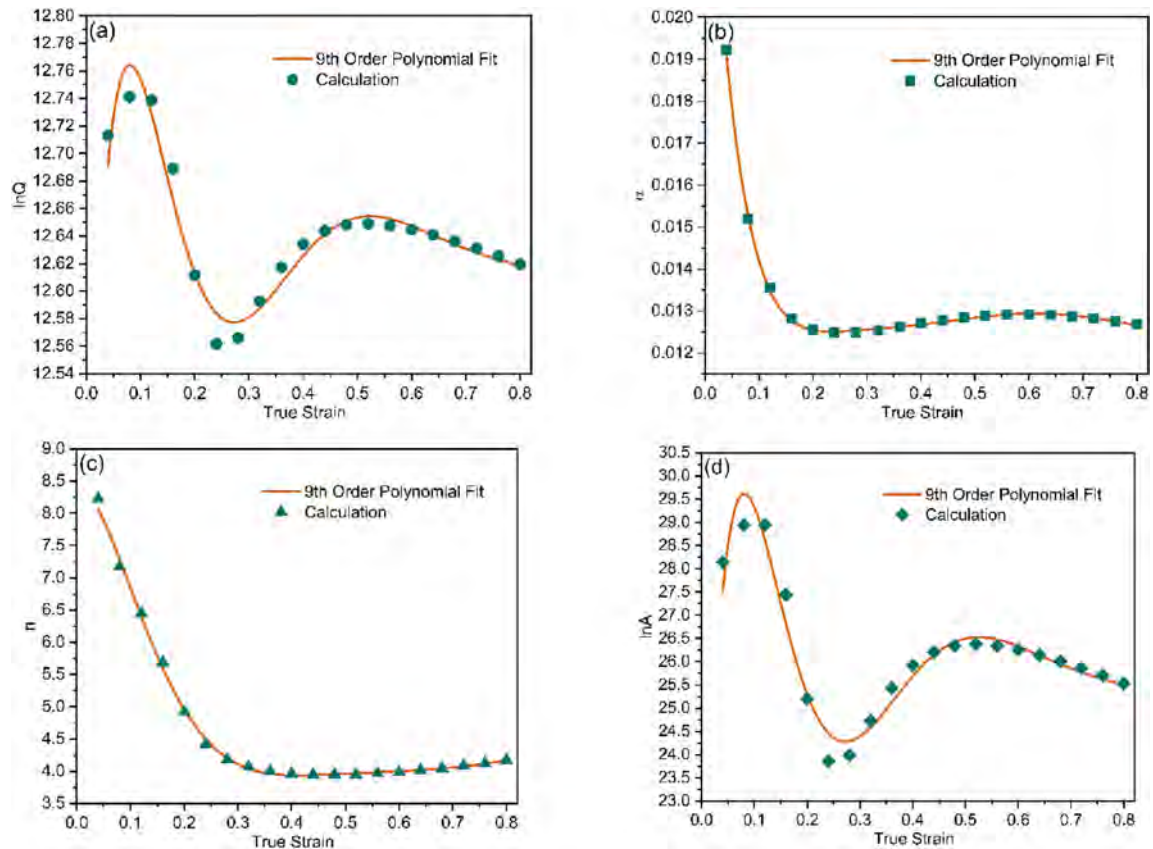


Fig. 18 – Fitting process of (a) $\ln Q$, (b) α , (c) n , (d) $\ln A$.

Avrami DRX kinetic model, which can be expressed as follows:

$$X_{\text{DRX}} = 1 - \exp\left(-b_0 \left(\frac{\varepsilon - \varepsilon_c}{\varepsilon_p}\right)^{k_0}\right) \quad (16)$$

where b_0 , k_0 are the material constants obtained by fitting. To facilitate the process, Eq. (16) should be transformed as:

$$\ln[-\ln(1 - X_{\text{DRX}})] = \ln b_0 + k_0 \ln\left(\frac{\varepsilon - \varepsilon_c}{\varepsilon_p}\right) \quad (17)$$

In previous studies, the values of b_0 , k_0 were usually obtained by fitting $\ln[-\ln(1 - X_{\text{DRX}})]$ and $\ln\left(\frac{\varepsilon - \varepsilon_c}{\varepsilon_p}\right)$ at a fixed strain

rate to establish a DRX kinetic model, approximately estimating the fraction of DRX under different deformation conditions. However, the accuracy of the prediction is inevitably affected. Therefore, by fitting $\ln[-\ln(1 - X_{\text{DRX}})]$ and $\ln\left(\frac{\varepsilon - \varepsilon_c}{\varepsilon_p}\right)$ at different strain rates respectively, the DRX kinetic model applicable to different deformation conditions was established:

$$X_{\text{DRX}} = \begin{cases} 1 - \exp\left(-2.5439 \left(\frac{\varepsilon - \varepsilon_c}{\varepsilon_p}\right)^{4.0605}\right) & (0\text{s}^{-1} < \dot{\varepsilon} \leq 0.01\text{s}^{-1}) \\ 1 - \exp\left(-1.1533 \left(\frac{\varepsilon - \varepsilon_c}{\varepsilon_p}\right)^{3.191}\right) & (0.01\text{s}^{-1} < \dot{\varepsilon} \leq 0.1\text{s}^{-1}) \\ 1 - \exp\left(-1.3272 \left(\frac{\varepsilon - \varepsilon_c}{\varepsilon_p}\right)^{2.7248}\right) & (0.1\text{s}^{-1} < \dot{\varepsilon} \leq 0.5\text{s}^{-1}) \\ 1 - \exp\left(-0.9817 \left(\frac{\varepsilon - \varepsilon_c}{\varepsilon_p}\right)^{2.5134}\right) & (0.5\text{s}^{-1} < \dot{\varepsilon} \leq 1\text{s}^{-1}) \end{cases} \quad (18)$$

Figs. 15 and 16 shows the comparison between the staged fitting model and the literature model [19], and the staged fitting model shows a good prediction accuracy.

Fig. 17(a) shows the DRX behavior at different temperatures at 0.5 s^{-1} . At the same temperature, the DRX behavior

Table 2 – Arrhenius constitutive model polynomial coefficients.

	$\ln Q$	α	n	$\ln A$
k_0	12.91454	0.02842	11.26399	33.87427
k_1	-12.9501	-0.33482	-135.698	-370.963
k_2	296.4088	3.25129	2069.36	8521.209
k_3	-3039.42	-18.8133	-18664.5	-87550.6
k_4	16222.98	69.7899	94929.94	468080.1
k_5	-49821.3	-169.056	-286055	-1439773
k_6	91727378	265.2459	523747.4	2654973
k_7	-100202	-259.294	-572857	-2904753
k_8	59948.1	143.351	344388.1	1740474
k_9	-15143.5	-34.1983	-87579.6	-440312

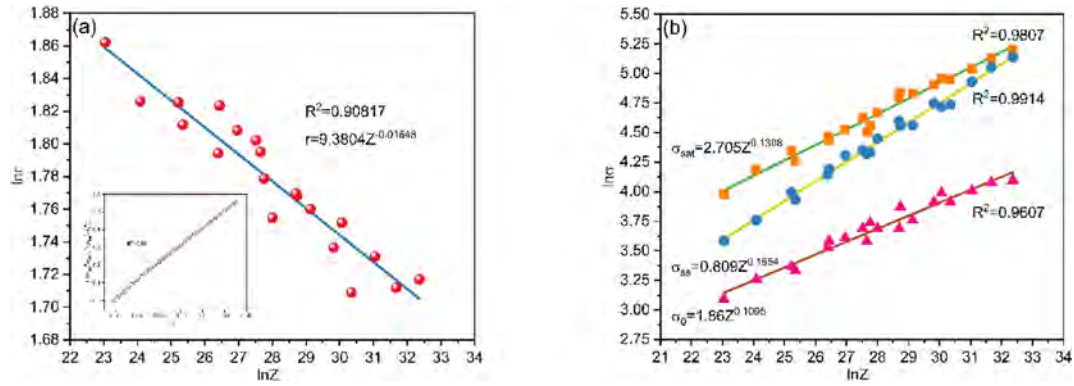


Fig. 19 – Relationship between (a) r and Z , (b) material characteristic value and Z .

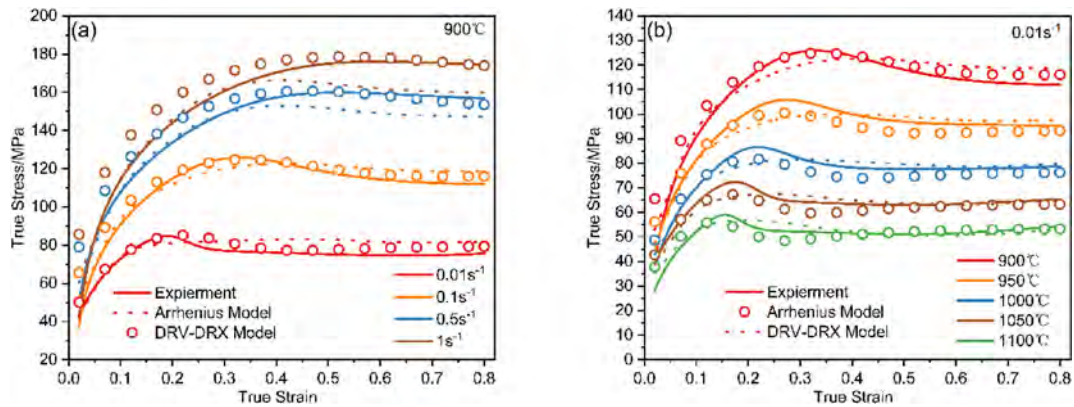


Fig. 20 – Comparison of predicted and experimental flow stress of two different models (a) in 900 °C with different strain rates, (b) in 0.01 s⁻¹ with different temperature.

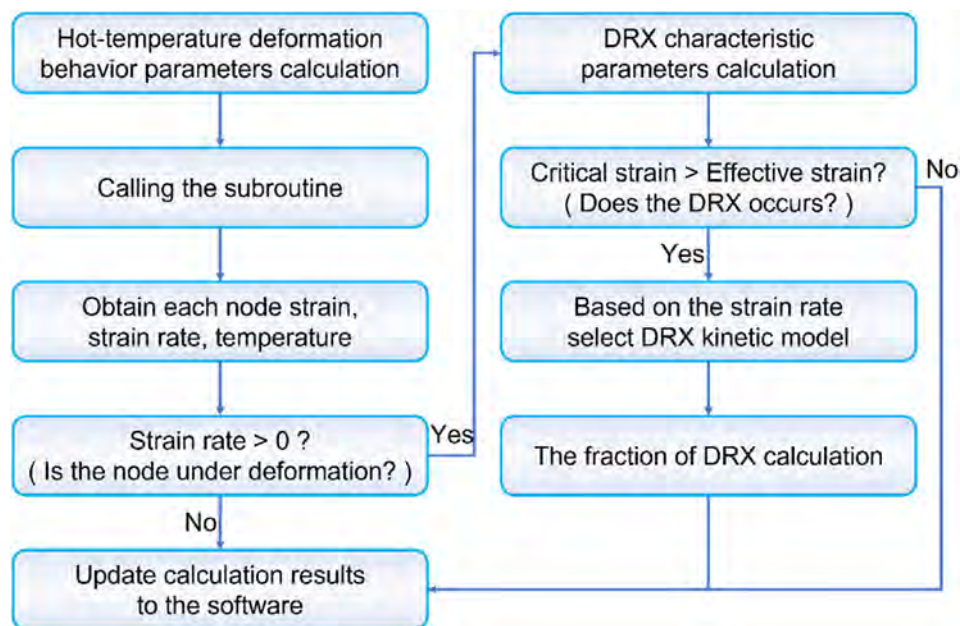


Fig. 21 – Subroutine flow chart.

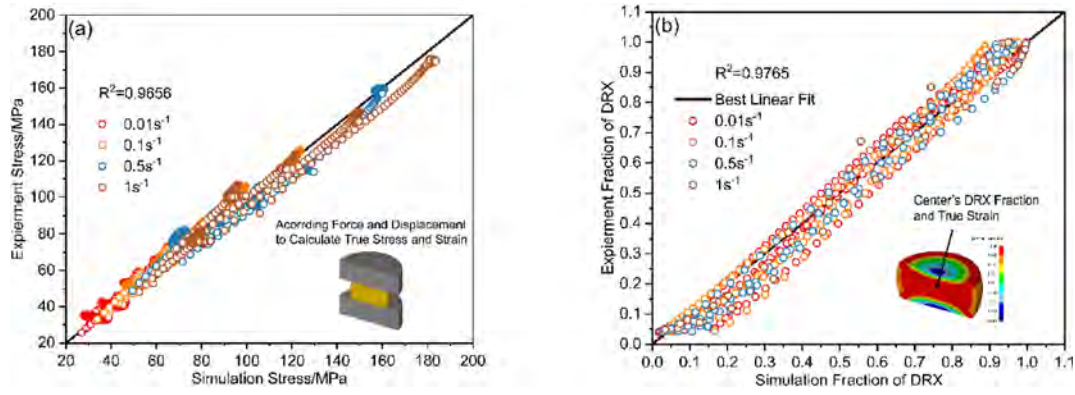


Fig. 22 – Comparison of simulation and experimental data of (a) flow stress, (b) fraction of DRX.

weakens with increasing strain rate, and the corresponding flow stress also shows a weakening softening effect [Fig. 6(a)]. Fig. 17(b) shows the DRX behavior at different strain rates at 900 °C. At the same strain rate, the DRX behavior weakens as the deformation temperature decreases, and the corresponding flow stress also shows a weakening softening effect [Fig. 6(b)]. These results indicate that low temperature and high strain rates are unfavorable for DRX behavior and the direct correspondence between DRX behavior and stress softening phenomena.

3.1.5. Constitutive model

Accurately describing the stress-strain relationship in the high-temperature deformation process of materials is the basis for the simulation of the machining process. It depends on the accurate establishment of the material constitutive model [14,23,72]. The Arrhenius constitutive model considering strain compensation and the DRV-DRX staged constitutive model considering material softening mechanism is widely used in steel materials. The two constitutive models

are represented as follows:

$$\begin{cases} \ln Q = k_0 + k_1 \epsilon + k_2 \epsilon^2 + k_3 \epsilon^3 + k_4 \epsilon^4 + k_5 \epsilon^5 \dots \\ \alpha = k_0 + k_1 \epsilon + k_2 \epsilon^2 + k_3 \epsilon^3 + k_4 \epsilon^4 + k_5 \epsilon^5 \dots \\ n = k_0 + k_1 \epsilon + k_2 \epsilon^2 + k_3 \epsilon^3 + k_4 \epsilon^4 + k_5 \epsilon^5 \dots \\ \ln A = k_0 + k_1 \epsilon + k_2 \epsilon^2 + k_3 \epsilon^3 + k_4 \epsilon^4 + k_5 \epsilon^5 \dots \\ \sigma = \frac{1}{\alpha} \ln \left\{ \left(\frac{Z}{A} \right)^{\frac{1}{n}} + \left[\left(\frac{Z}{A} \right)^{\frac{2}{n}} + 1 \right]^{\frac{1}{2}} \right\} \end{cases} \quad (19)$$

$$\begin{cases} \sigma = \sqrt{\sigma_{sat}^2 + (\sigma_0^2 - \sigma_{sat}^2) \exp(-\epsilon r)} (\epsilon < \epsilon_c) \\ \sigma = \sigma_{DRV} - (\sigma_{sat} - \sigma_{ss}) \left[1 - \exp \left(-k_0 \left(\frac{\epsilon - \epsilon_c}{\epsilon_p} \right)^{t_0} \right) \right] (\epsilon \geq \epsilon_c) \end{cases} \quad (20)$$

Establishing the Arrhenius constitutive model considering strain compensation is relatively simple. The material

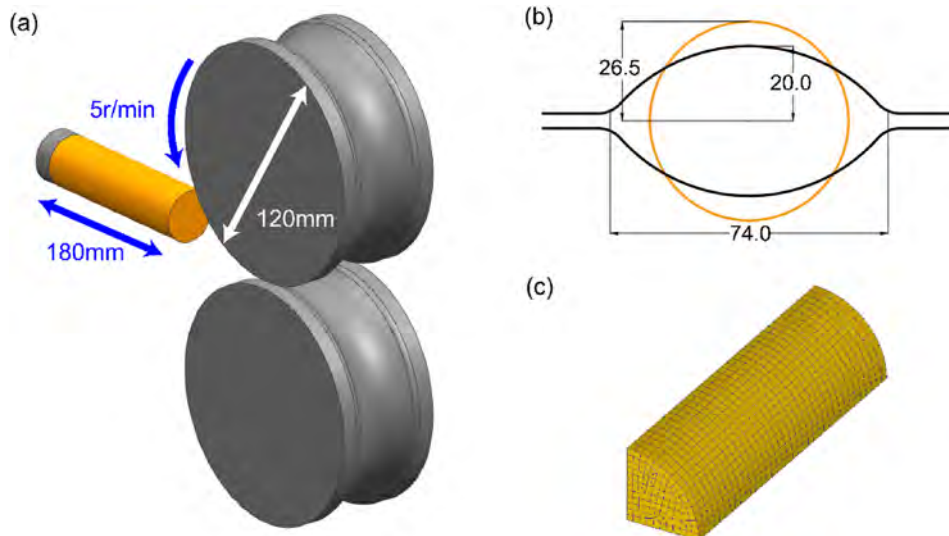


Fig. 23 – Finite-element model (a) 3D models in UG (b) roller hole size (c) bar's hexahedral meshes.

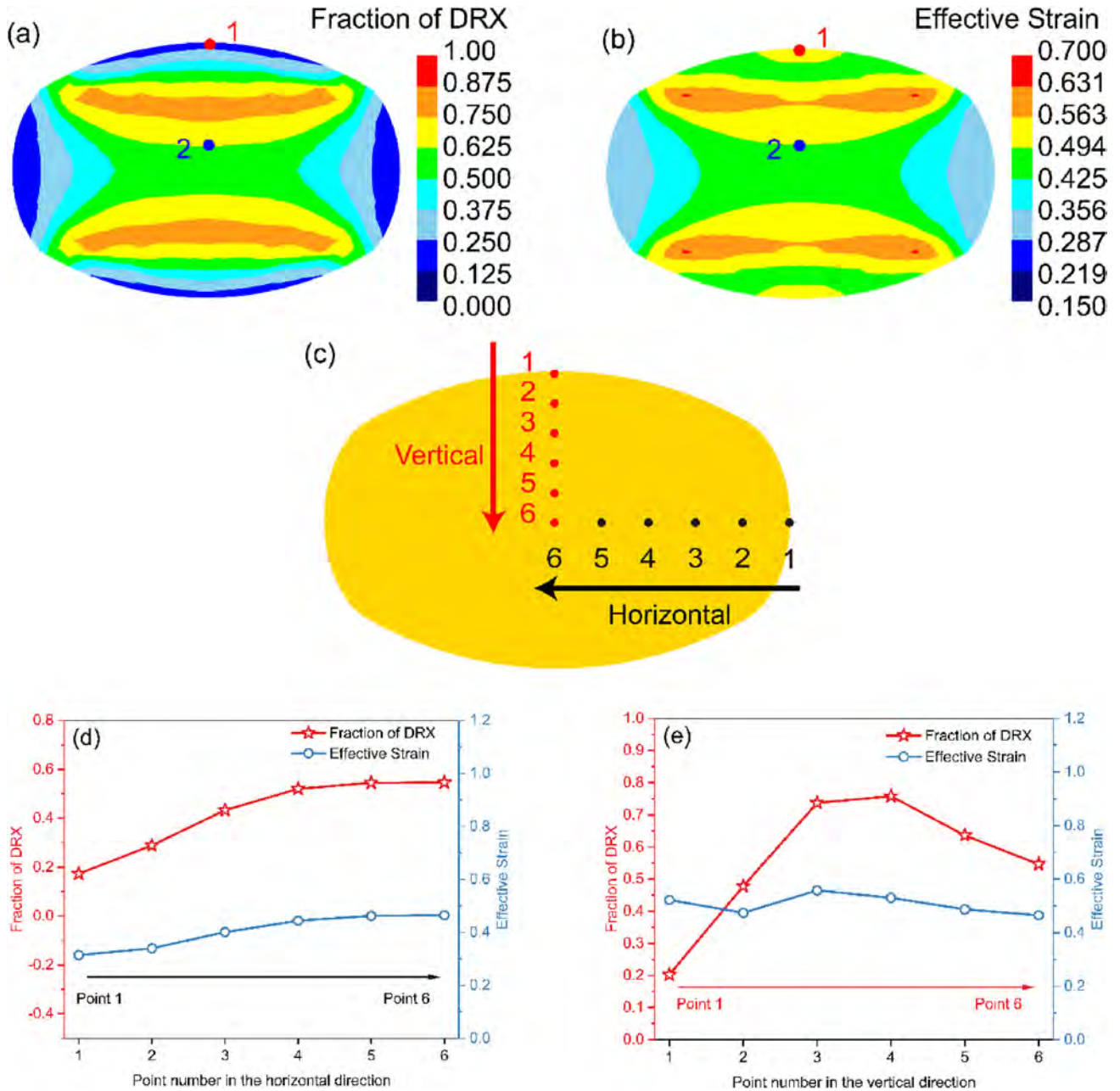


Fig. 24 – (a) the fraction of DRX after rolling, (b) effective strain after rolling, (c) schematic diagram of selected points in vertical and horizontal direction, (d) the fraction of DRX and effective strain in horizontal direction, (e) the fraction of DRX and effective strain in vertical direction.

coefficients under different strains are obtained, and polynomial fitting is performed. The fitting process is shown in Fig. 18, and the polynomial coefficients are shown in Table 2.

Establishing the DRV-DRX staged constitutive model considering the material softening mechanism is relatively complicated. Establishing the relationship between the material characteristic parameters, the softening coefficient r , and Z is necessary. This paper uses a new method to solve the softening coefficient [30]. Based on the σ_{DRV} solution method proposed by Zahiri [71], σ_{DRV} is first obtained, and the solution process is detailed above. Moreover, according to the formula, the softening coefficient r is solved.

$$r = \frac{\ln\left(\frac{\sigma_{sat}^2 - \sigma_{DRV}^2}{\sigma_{sat}^2 - \sigma_0^2}\right)}{\varepsilon} \quad (\varepsilon < \varepsilon_c) \quad (21)$$

where σ_0 is the yield stress, the stress value under the true strain of 0.02 is taken here. Fig. 19 shows the relationship between material eigenvalues, softening coefficient, and Z .

Fig. 20 compares the accuracy of two constitutive models under different deformation conditions. The DRV-DRX staged constitutive model, considering the material softening mechanism, is more accurate for describing the flow stress curves of different softening mechanisms. For example, when

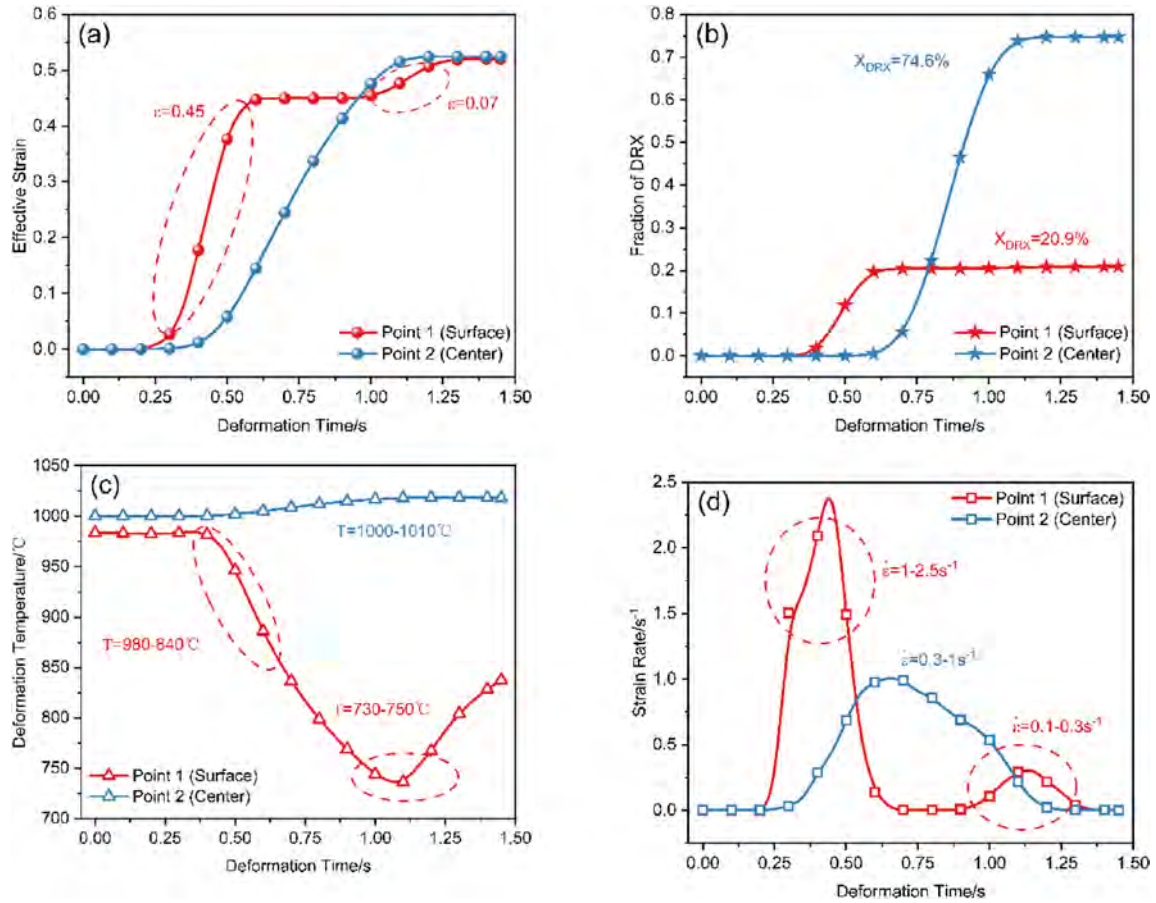


Fig. 25 – (a) the effective strain change, (b) the fraction of DRX change, (c) the deformation temperature change, (d) the strain rate change of two points during hot rolling process.

the strain rate at 900 °C changes from 0.01 s⁻¹ to 1 s⁻¹, the softening mechanism changes from DRX to DRV. The DRV-DRX staged constitutive model is in good agreement. This may be attributed to the fact that the Arrhenius constitutive model considering strain compensation fits the flow stress curves of different softening mechanisms and does not consider the physical significance of the changes in the softening mechanism. Therefore, this paper adopts the DRV-DRX staged constitutive model to describe the high-temperature deformation behavior of the material.

3.2. Numerical simulation

3.2.1. Material model embedding and validation

To simulate the DRX behavior in the hot rolling process, the material constitutive and DRX dynamics models are embedded in finite element software. In calculating the DRX volume fraction, it is first to determine whether deformation occurs and whether the equivalent strain is greater than the critical strain. When the DRX behavior occurs, the DRX dynamic model coefficients will be selected according to the deformation conditions, and the DRX volume fraction will be calculated incrementally. The specific formula is as follows, and the calculation process is shown in Fig. 21.

$$dX_{DRX} = \left(-b_0 \exp \left(\left(\frac{\epsilon - \epsilon_c}{\epsilon_p} \right)^{k_0} \right) \right) \left(-\frac{b_0 k_0}{\epsilon_p} \exp \left(\left(\frac{\epsilon - \epsilon_c}{\epsilon_p} \right)^{k_0 - 1} \right) \right) d\epsilon \quad (22)$$

$$X_{DRX}^{i+1} = X_{DRX}^i + dX_{DRX} \quad (23)$$

In order to ensure the accuracy of the model, the hot compression test process was simulated. The flow stress and DRX volume fraction under different deformation conditions were compared between the simulated and experimental values, as shown in Fig. 22, and the agreement was satisfactory.

3.2.2. Finite-element model

In this paper, based on the actual situation, a finite element model of bar single-pass hot rolling is established by Deform-3D software to simulate the DRX behavior of the bar under the round-oval hole type system. Fig. 23(a) shows the model established by UG software, and the dimension of the bar is a diameter of 53 mm and a length of 180 mm. The size of the roller is a diameter of 120 mm, slot hole depth of 40 mm, slot hole width of 74 mm, roll spacing of 8 mm, and the roller speed is 5 r/min. Fig. 23(b) shows the hole size of the roller. Due to the symmetry of the bar, the 1/4 model was imported

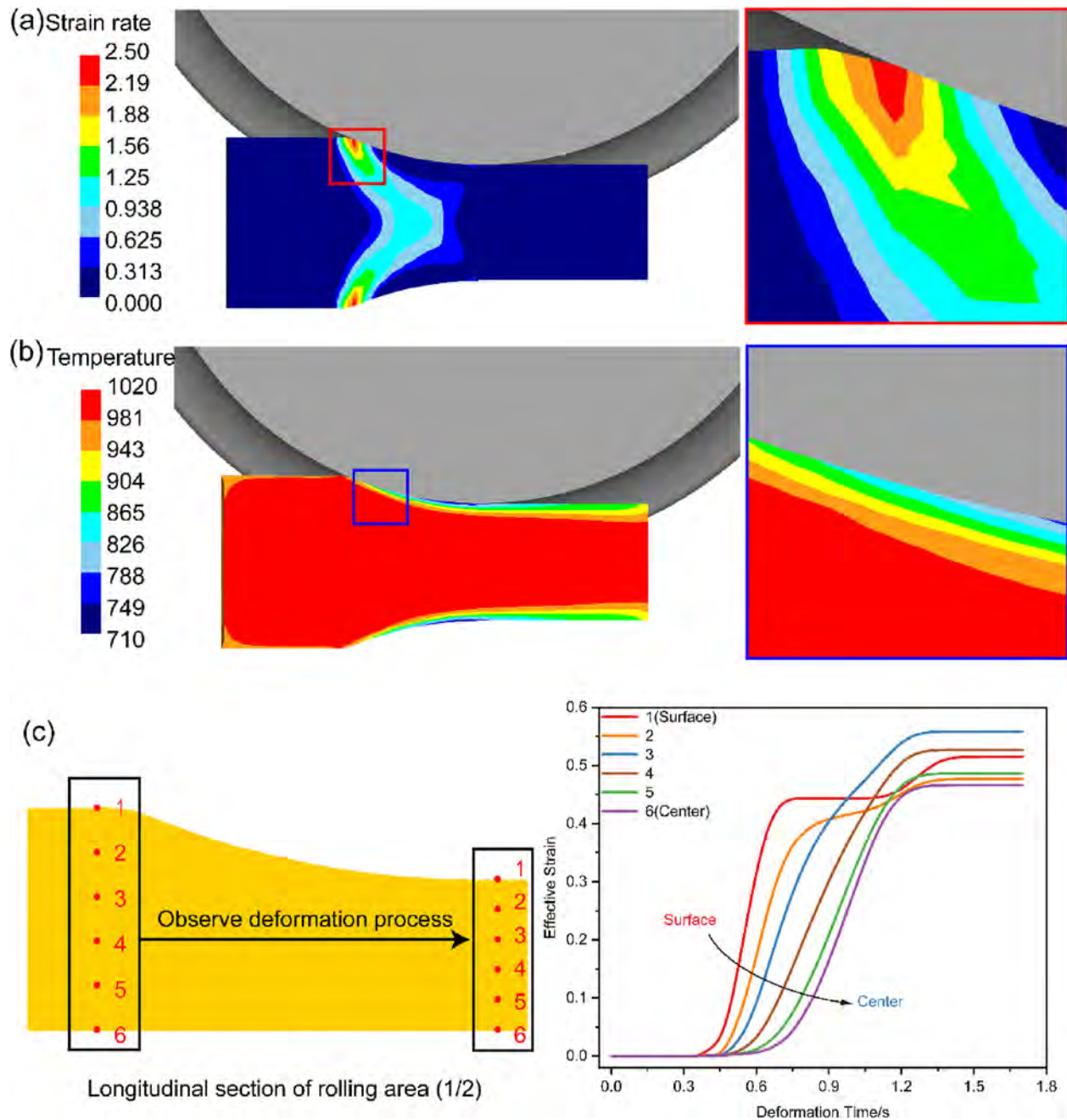


Fig. 26 – (a) strain rate distribution in rolling region (b) deformation temperature distribution in rolling region (c) the effective strain change of the equally spaced six points in the vertical direction.

into DEFORM-3D set as rigid-plastic bodies with 5000 hexahedral meshes. The rollers are set as rigid bodies without meshing. The initial temperature of the bar and the rollers are 1000 °C and 20 °C. The heat transfer coefficient between the bar and the rollers and the environment is 5 Kw/(m²·k) and 0.02 Kw/(m²·k). The friction relationship between the bar and the rollers is shear friction with a friction coefficient of 0.3. The bar's cross-section transforms from a circular to an elliptical through the rolling process.

Table 3 – Simulation of rolling conditions.

Simulation group	Rolling temperature	Roller speed
1	900 °C	5r/min
2	1000 °C	5r/min
3	1100 °C	1r/min
4	1000 °C	5r/min
5	1000 °C	20r/min

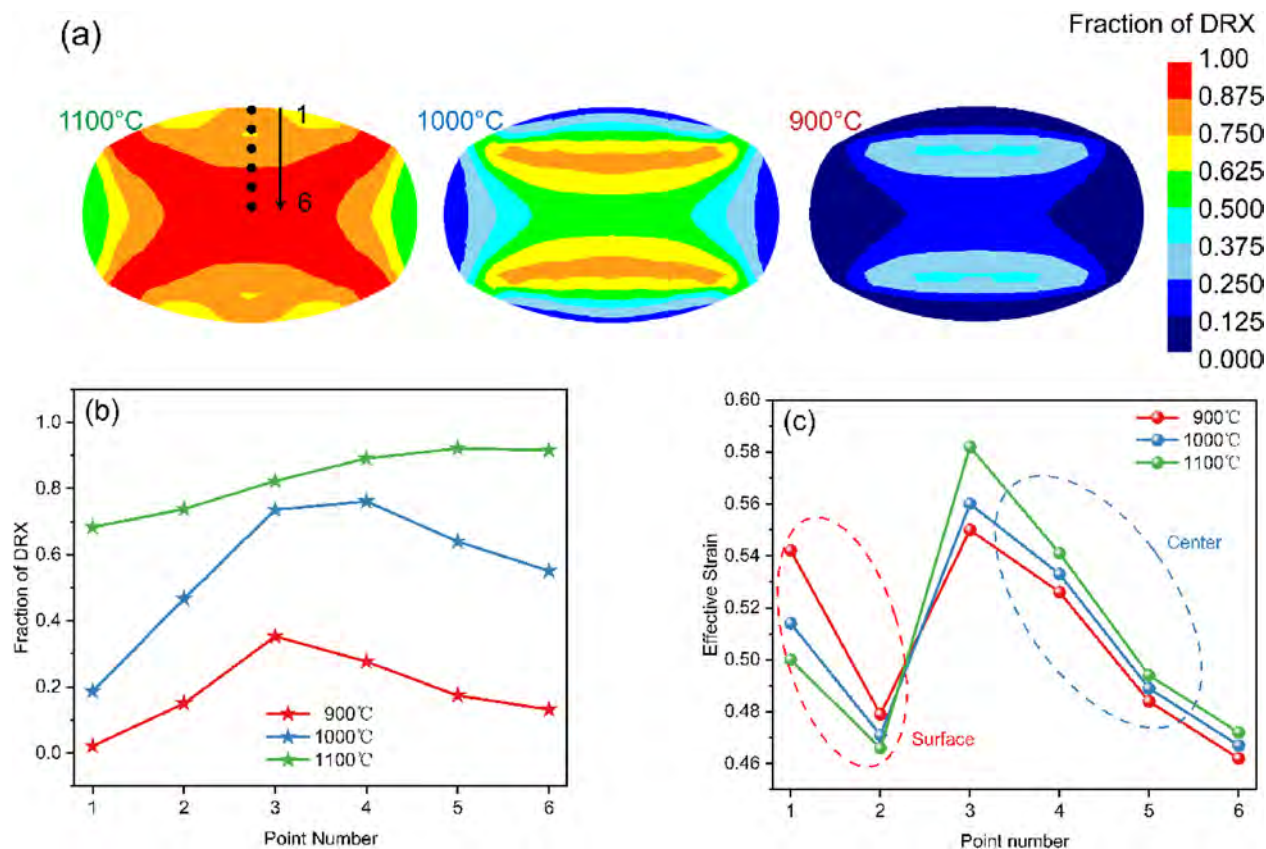


Fig. 27 – (a) distribution of the fraction of DRX at different rolling temperatures (b) the fraction of DRX in vertical direction (c) the effective strain in vertical direction.

3.2.3. DRX non-uniformity phenomenon

Fig. 24(a) shows the non-uniformity distribution of the fraction of DRX of the cross-section after rolling at a rolling temperature of 1000 °C, with a roller speed of 5r/min. In the vertical direction (the main deformation direction in direct contact with the roller), the fraction of DRX increases from the surface to the center and then decreases. However, In the horizontal direction (not in direct contact with the roller) the fraction of DRX gradually increases from the surface to the center. Fig. 24(b) shows the effective strain of the bar's cross-section after rolling. The distribution of the effective strain in vertical direction from the center to the surface is not significantly different. The maximum deformation occurs in the area between the surface and the center. However, the effective strain gradually decreases horizontally from the surface to the center. The deformation energy is the driving force of DRX behavior [73,74]. Therefore, the deformation non-uniformity can explain the DRX inhomogeneity behavior in the horizontal direction. Fig. 24(d) shows the six equally spaced points fraction of DRX in the horizontal direction and the effective strain, and there is a correspondence between them in this direction. The shape rolling characteristics caused the deformation to gradually increase horizontally from the center to the surface, leading to the non-uniformity DRX behavior. Fig. 24(e) shows the six equally spaced points of the fraction of DRX and the effective strain in the vertical direction. There is no direct relationship between the

deformation and the fraction of DRX in the surface area. Even though there is no significant difference between the deformation occurring in the surface and the center, the surface DRX's ability is significantly weaker than the center. However, the fraction of DRX in the center corresponds to the deformation. With the deformation decreasing, the fraction of DRX decreases. The weak surface ability of DRX in the vertical direction has a significantly adverse effect on the performance of the production. The arrangement of shape rolling caused the main deformation direction of the current pass will become the non-major deformation direction in the next pass. If the sufficient deformation cannot activate an adequate DRX behavior in this region, it cannot refine the grains by DRX behavior affecting the final product performance. This paper will explain the phenomenon and the behavior under different rolling processes.

To explain this phenomenon, two points with the same degree of deformation and a significant difference in the fraction of DRX were chosen to observe the deformation process. Fig. 24(a) shows the position of the points. Fig. 25(a) shows the effective strain change of the points during the deformation. The deformation of the surface point is composed of a high strain rate significant degree of deformation, and a low strain rate small degree of deformation. The surface point deforms before the center point but lags the center to reach an equal deformation degree. Fig. 25(b) shows the fraction of DRX change during the deformation of the two

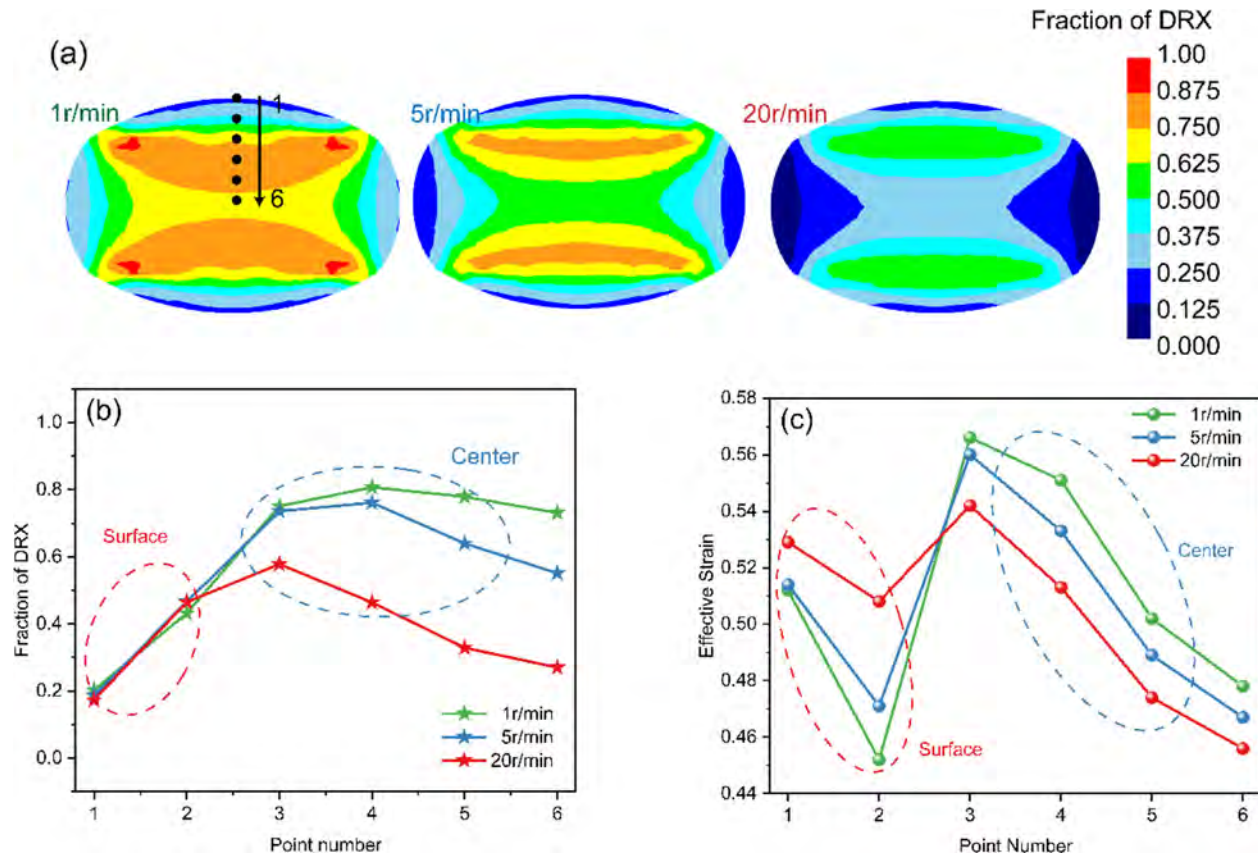


Fig. 28 – (a) distribution of the fraction of DRX at different roller speeds (b) the fraction of DRX in vertical direction (c) the effective strain in vertical direction.

points. The surface DRX ability is significantly weaker than the center, and the DRX behavior hardly occurs during the second deformation of the surface. Fig. 25(c) shows the change in deformation temperature of the two points. The surface point deformation temperature is 980°C–840 °C during the first deformation process and decreases to 740°C–765 °C when the second deformation occurs due to the heat transfer between the rollers and the bar. The surface point deformation temperature maintains between 1000°C and 1010 °C, and a slight temperature rise is caused by deformation. From the previous discussion, the low temperature can significantly inhibit the DRX ability by weakening the atomic diffusion. Therefore, the heat transfer between the surface area and the rollers is a reason for the difference in the fraction of DRX under the same deformation. Fig. 25(d) shows the strain rate change during the deformation of the two points. The strain rate during the first deformation ($1\text{s}^{-1} - 2.5\text{s}^{-1}$) of the surface point due to the forced deformation caused by direct contact with the rollers is significantly higher than the strain rate of the center point ($0.3\text{s}^{-1} - 1\text{s}^{-1}$). The increased strain rate will lead to insufficient time for the DRX behavior, which will significantly inhibit the DRX behavior. Therefore, the high strain rate of the surface is also a reason for the difference in the fraction of DRX at the same deformation degree. Even the low strain rate can provide sufficient time for DRX behavior during the surface's second deformation process. However, due to the minor effective strain (0.07) and the low

deformation temperature (740°C–765 °C), DRX behavior does not occur during the second deformation. Therefore, the low deformation temperature, high strain rate, and discontinuous deformation phenomenon caused by direct contact between the surface area and the rollers are the significant difference in the fraction of DRX between the surface and the center when the same degree of deformation occurs in these two areas.

Discontinuous deformation of the surface area during the rolling process is a particular phenomenon, but no analysis has given a specific reason [17,19,75,76]. Since the discontinuous deformation phenomenon is a reason for the low surface fraction of DRX, this paper will investigate the causes. Fig. 26(a) and (b) show the rolling region's strain rate and deformation temperature. The surface strain rate is significantly higher than the center, and the deformation temperature is lower than the center. Fig. 26(c) shows the six equally spaced points' deformation process from the center to the surface in the vertical direction. The center deformation precedes the surface area. The closer the surface, the earlier the deformation occurs, indicating that the deformation is a gradual penetration process from the surface to the center. High strain rate and low deformation temperature during surface deformation, resulting in rapid hardening and difficulty in continuing deformation. Therefore, more deformation occurs in the center, and an intermediate non-deformation process appears on the surface. However, with

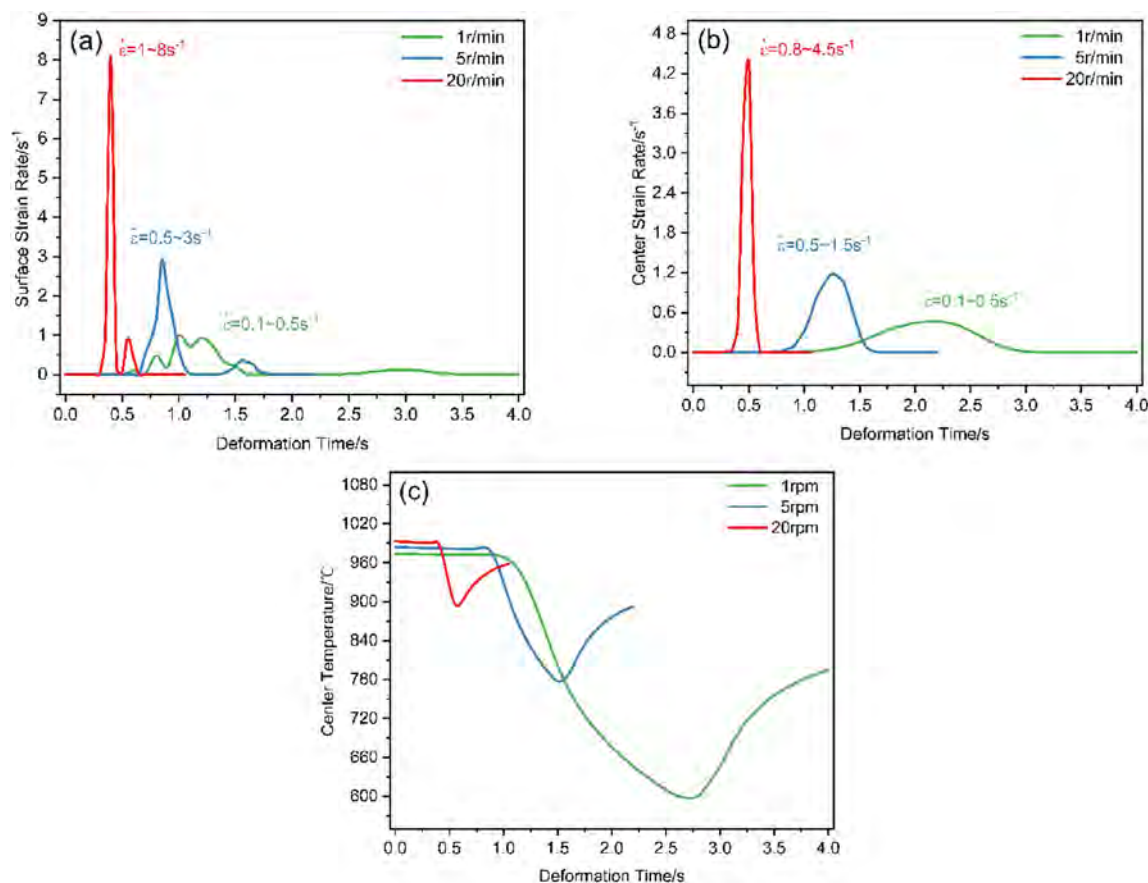


Fig. 29 – (a) the surface strain rate change (b) the center strain rate change (c) the surface temperature change during rolling process at different roller speeds.

the center's deformation gradually increasing, the center hardened, and further deformation was difficult. Therefore, deformation will occur in the surface area again, resulting in discontinuous surface deformation.

3.2.4. The fraction of DRX non-uniformity in different rolling processes

The rolling temperature and the roller speed are the main factors affecting the DRX behavior. Table 3 shows the simulated rolling conditions. By comparing the simulation results of 1, 2, and 3, the effect of rolling temperature on the non-uniformity of DRX degree is investigated. By comparing the simulation results of 2, 4, and 5, the effect of roller speed on the non-uniformity of DRX degree is investigated. By summarizing the non-uniformity DRX behavior under different rolling processes, a theoretical basis can be obtained for the suitable rolling process.

Fig. 27(a) shows the fraction of DRX of the cross-section after rolling at different rolling temperatures. With the increase in rolling temperature from 900 °C to 1100 °C, the fraction of DRX of the bar is significantly raised, and the uniformity of the rolled section is improved to a great extent. To characterize the variation of DRX non-uniformity in the vertical direction at different rolling temperatures, six points were selected at equal intervals from the surface to the center to observe the fraction of DRX after rolling. The results are shown in Fig. 27(b). At 1100 °C, there is a significant

improvement in DRX non-uniformity in the vertical direction. A substantial enhancement in DRX ability occurs in the surface area in direct contact with the rollers. As the rolling temperature increases, the surface area deformation temperature can still maintain at a high level; even the temperature will decrease due to direct contact heat exchange with the rollers, ensuring the DRX ability of the area. Fig. 27(c) shows the six points of effective strain after rolling at different rolling temperatures. With the increase in rolling temperature, the deformation will be more concentrated in the center of the bar. As the rolling temperature increases, the center area deforms more efficiently at high temperatures due to the surface's rapid hardening during the deformation process, resulting in the deformation concentration in the center.

Fig. 28(a) shows the distribution of the fraction of DRX of the cross-section after rolling at different roller speeds. With the decrease in roller speed from 20r/min to 1r/min, there is a significant increase in the degree of DRX in the center of the bar after rolling, but no notable change occurs in the surface area. To characterize the variation of DRX non-uniformity in the vertical direction at different rolling temperatures, six points were selected at equal intervals from the surface to the center in this direction to observe the fraction of DRX after rolling. Fig. 28(b) shows that when the roll speed is reduced from 20r/min to 1r/min, the fraction of DRX in the center increases from 0.3 to 0.6 to about 0.8, while the surface maintains between 0.2 and 0.5. This phenomenon is because the

decrease in roller speed affects the surface and center's thermal deformation behavior. The roller speed decrease significantly reduces the center strain rate. Fig. 29(b) shows that when the roller speed decreases from 20r/min to 1r/min, the strain rate of the deformation process in the center decreases from 0.8 s^{-1} – 4.5 s^{-1} to 0.1 s^{-1} – 0.5 s^{-1} . The sufficient time for DRX increases the fraction of DRX in the center. For the surface area, the roller speed decrease reduces the strain rate and increases the contact time with the rollers but increasing the heat transfer time between the surface and the roller. Fig. 29(a), (c) shows that although the surface strain rate of the deformation process decreases from 1 s^{-1} – 8 s^{-1} to 0.1 s^{-1} – 0.5 s^{-1} , Lower deformation temperature counteracts the contribution of reduced strain rate to DRX behavior, resulting in little change in the fraction of DRX. Fig. 28(c) shows the effective strain after rolling at 1–6 points with different roller speeds. As the roller speed decreases from 20r/min to 1r/min, the surface deformation degree will reduce, and the center deformation degree will increase. As the roller speed decreases, the contact time between the bar and the roll is extended, and the heat exchange is adequate, resulting in the surface deformation temperature decreasing. Therefore, the deformation in the center is more difficult, and the deformation will be assumed by the center more.

4. Conclusion

Based on physical and numerical simulation, this paper investigates the flow stress curve of a low carbon steel under deformation temperature of 900°C – 1100°C and strain rate of 0.01 s^{-1} – 1 s^{-1} . The mechanism of the DRX behavior during high-temperature deformation is illustrated. The DRX kinetic model for different deformation conditions is established. Then the DRX dynamics model is embedded in the finite element software to investigate the phenomenon and causes of non-uniformity of DRX degree in bar rolling under a single pass. Moreover, the performance of this phenomenon under different rolling processes is investigated. The main conclusions are as follows:

- (1) Considering the direct effect of deformation conditions on DRX behavior, a DRX kinetic model applicable to different deformation conditions was established. Compared with the conventional DRX kinetic model, the high agreement between predicted and experimental data indicates the accuracy of the DRX kinetic model.
- (2) The DRX behavior of a hot-rolled bar was simulated using finite-element software; the results show that the fraction of DRX after rolling exhibits significant non-uniformity. This phenomenon is caused by the non-uniform deformation caused by the characteristics of type rolling and the surface area's low temperature, high strain rate, and discontinuous deformation caused by the direct contact with the rolls during the deformation process.
- (3) Increasing the rolling temperature can significantly improve the DRX non-uniformity and increase the overall DRX degree. Decreasing the roller speed has a different effect on the surface and the center. The reduced strain rate improves the fraction of DRX for the center area,

providing adequate DRX behavior time. Even decreasing the roller speed reduces the surface strain rate for the surface area. The contact heat exchange time increases the deformation temperature, resulting in no significant change in the fraction of DRX in the surface area.

Declaration of Competing Interest

The authors declare that they have no known competing financial interests or personal relationships that could have appeared to influence the work reported in this paper.

Acknowledgments

This work was supported by Regional Joint Funds of the National Natural Science Foundation of China (Grant No. U20A20289); Innovative Research Groups Project of the Natural Science Foundation of Hebei Province (Grant No. E2021203011). Innovative Capacity Cultivation Funding Project for Postgraduates of Hebei Province (Grant No. CXZZSS20221).

REFERENCES

- [1] Zhao R-J, Fu J-X, Wu Y-X, Yang Y-J, Zhu Y-Y, Zhang M. Representative technologies for hot charging and direct rolling in global steel industry. *ISIJ Int* 2015;55:1816–21. <https://doi.org/10.2355/isijinternational.ISIJINT-2015-175>.
- [2] Oezguer A, Uygun Y, Huett M-T. A review of planning and scheduling methods for hot rolling mills in steel production. *Comput Ind Eng* 2021;151:106606. <https://doi.org/10.1016/j.cie.2020.106606>.
- [3] Kodukula S, Kokkomaki H, Puukko E, Porter D, Komi J. Influence of hot rolling finishing temperature on texture and ridging resistance in stabilized ferritic stainless steels. *Steel Res Int* 2021;92:2000695. <https://doi.org/10.1002/srin.202000695>.
- [4] Na T-W, Park H-K, Park C-S, Joo H-D, Park J-T, Han HN, et al. Effect of asymmetric hot rolling on the texture evolution of Fe-3%Si steel. *Met Mater Int* 2018;24:1369–75. <https://doi.org/10.1007/s12540-018-0145-0>.
- [5] Xu SC, Wang LD, Li HB, Qu CQ, Fei WD. Effects of rolling temperature on hot rolling behaviors and mechanical properties of ABOw/6061Al composites. *Mater Sci Eng -Struct Mater Prop Microstruct Process* 2014;615:208–13. <https://doi.org/10.1016/j.msea.2014.07.021>.
- [6] Liu C, Barella S, Peng Y, Sun J, Guo S, Liang S, et al. Dynamic recrystallization behavior under steady and transient mutation deformation state. *Mater Sci Eng, A* 2022:143138. <https://doi.org/10.1016/j.msea.2022.143138>.
- [7] Ji H, Cai Z, Pei W, Huang X, Lu Y. DRX behavior and microstructure evolution of 33Cr23Ni8Mn3N: experiment and finite element simulation. *J Mater Res Technol-Jmrt* 2020;9:4340–55. <https://doi.org/10.1016/j.jmrt.2020.02.059>.
- [8] Li J, Liu Y, Wang Y, Liu B, He Y. Dynamic recrystallization behavior of an as-cast TiAl alloy during hot compression. *Mater Char* 2014;97:169–77. <https://doi.org/10.1016/j.matchar.2014.09.013>.
- [9] Babu KA, Mandal S, Athreya CN, Shakthipriya B, Sarma VS. Hot deformation characteristics and processing map of a

- phosphorous modified super austenitic stainless steel. *Mater Des* 2017;115:262–75. <https://doi.org/10.1016/j.matdes.2016.11.054>.
- [10] Liu C, Mapelli C, Peng Y, Barella S, Liang S, Gruttadauria A, et al. Dynamic recrystallization behavior of low-carbon steel during the flexible rolling process: modeling and characterization. *Steel Res Int* 2022;2100490. <https://doi.org/10.1002/srin.202100490>.
 - [11] Zhu S, Cao H, Ye J, Hu W, Zheng G. Dynamic recrystallization behavior of medium carbon Cr-Ni-Mo-Nb steel during hot deformation. *J Iron Steel Res Int* 2015;22:264–71. [https://doi.org/10.1016/S1006-706X\(15\)60040-1](https://doi.org/10.1016/S1006-706X(15)60040-1).
 - [12] Han Y, Yan S, Yin B, Li H, Ran X. Effects of temperature and strain rate on the dynamic recrystallization of a medium-high-carbon high-silicon bainitic steel during hot deformation. *Vacuum* 2018;148:78–87. <https://doi.org/10.1016/j.vacuum.2017.11.007>.
 - [13] Kumar SSS, Raghu T, Bhattacharjee PP, Rao GA, Borah U. Strain rate dependent microstructural evolution during hot deformation of a hot isostatically processed nickel base superalloy. *J Alloys Compd* 2016;681:28–42. <https://doi.org/10.1016/j.jallcom.2016.04.185>.
 - [14] Wang X, Chandrashekhara K, Rummel SA, Lekakh S, Van Aken DC, O'Malley RJ. Modeling of mass flow behavior of hot rolled low alloy steel based on combined Johnson-Cook and Zerilli-Armstrong model. *J Mater Sci* 2017;52:2800–15. <https://doi.org/10.1007/s10853-016-0570-8>.
 - [15] Nalawade RS, Puranik AJ, Balachandran G, Mahadik KN, Balasubramanian V. Simulation of hot rolling deformation at intermediate passes and its industrial validity. *Int J Mech Sci* 2013;77:8–16. <https://doi.org/10.1016/j.ijmecsci.2013.09.017>.
 - [16] Kim SY, Im YT. Three-dimensional finite element analysis of non-isothermal shape rolling. *J Mater Process Technol* 2002;127:57–63. [https://doi.org/10.1016/S0924-0136\(02\)00256-X](https://doi.org/10.1016/S0924-0136(02)00256-X).
 - [17] Ding H, Hirai K, Homma T, Kamado S. Numerical simulation for microstructure evolution in AM50 Mg alloy during hot rolling. *Comput Mater Sci* 2010;47:919–25. <https://doi.org/10.1016/j.commatsci.2009.11.024>.
 - [18] Gu S, Zhang L, Yue C, Ruan J, Zhang J, Gao H. Multi-field coupled numerical simulation of microstructure evolution during the hot rolling process of GCr15 steel rod. *Comput Mater Sci* 2011;50:1951–7. <https://doi.org/10.1016/j.commatsci.2011.01.034>.
 - [19] Wang X, Chandrashekhara K, Lekakh SN, Van Aken DC, O'Malley RJ. Modeling and simulation of dynamic recrystallization behavior in alloyed steel 15V38 during hot rolling. *Steel Res Int* 2019;90:1700565. <https://doi.org/10.1002/srin.201700565>.
 - [20] Mirzadeh H, Cabrera JM, Najafizadeh A. Constitutive relationships for hot deformation of austenite. *Acta Mater* 2011;59:6441–8. <https://doi.org/10.1016/j.actamat.2011.07.008>.
 - [21] Bhattacharya R, Lan YJ, Wynne BP, Davis B, Rainforth WM. Constitutive equations of flow stress of magnesium AZ31 under dynamically recrystallizing conditions. *J Mater Process Technol* 2014;214:1408–17. <https://doi.org/10.1016/j.jmatprotec.2014.02.003>.
 - [22] Spigarelli S, El Mehtedi M, Ricci P, Mapelli C. Constitutive equations for prediction of the flow behaviour of duplex stainless steels. *Mater Sci Eng, A* 2010;527:4218–28. <https://doi.org/10.1016/j.msea.2010.03.029>.
 - [23] Liu Q, Tian Y, Zhai J, Tian L, Chen L, Chen L. Prediction of surface wrinkle defect of welding wire steel ER70S-6 in hot bar rolling process using finite element method and experiments. *Metals* 2020;10:1559. <https://doi.org/10.3390/met10111559>.
 - [24] Wang X, Chandrashekhara K, Buchely MF, Lekakh S, Van Aken DC, O'Malley RJ, et al. Experiment and simulation of static softening behavior of alloyed steel during round bar hot rolling. *J Manuf Process* 2020;52:281–8. <https://doi.org/10.1016/j.jmapro.2020.02.031>.
 - [25] Jung KH, Lee HW, Im YT. A microstructure evolution model for numerical prediction of austenite grain size distribution. *Int J Mech Sci* 2010;52:1136–44. <https://doi.org/10.1016/j.ijmecsci.2009.09.010>.
 - [26] Liu G, Han Y, Shi Z, Sun J, Zou D, Qiao G. Hot deformation and optimization of process parameters of an as-cast 6Mo superaustenitic stainless steel: a study with processing map. *Mater Des* 2014;53:662–72. <https://doi.org/10.1016/j.matdes.2013.07.065>.
 - [27] Han Y, Liu G, Zou D, Liu R, Qiao G. Deformation behavior and microstructural evolution of as-cast 904L austenitic stainless steel during hot compression. *Mater Sci Eng, A* 2013;565:342–50. <https://doi.org/10.1016/j.msea.2012.12.043>.
 - [28] Han Y, Liu GW, Zou DN, Sun JP, Qiao GJ. Investigation on hot deformation of 20Cr–25Ni superaustenitic stainless steel with starting columnar dendritic microstructure based on kinetic analysis and processing map. *Mater Sci Technol* 2013;29:300–8. <https://doi.org/10.1179/1743284712Y.0000000145>.
 - [29] Wan Z, Sun Y, Hu L, Yu H. Dynamic softening behavior and microstructural characterization of TiAl-based alloy during hot deformation. *Mater Char* 2017;130:25–32. <https://doi.org/10.1016/j.matchar.2017.05.022>.
 - [30] Liu C, Peng Y, Barella S, Mapelli C, Liang S. Characterization of dynamic recrystallization behavior of low carbon steel under flexible rolling process. *Mater Today Commun* 2021;29:102777. <https://doi.org/10.1016/j.mtcomm.2021.102777>.
 - [31] Jonas JJ, Queleennec X, Jiang L, Martin É. The Avrami kinetics of dynamic recrystallization. *Acta Mater* 2009;57:2748–56. <https://doi.org/10.1016/j.actamat.2009.02.033>.
 - [32] Li X, Duan L, Li J, Wu X. Experimental study and numerical simulation of dynamic recrystallization behavior of a micro-alloyed plastic mold steel. *Mater Des* 2015;66:309–20. <https://doi.org/10.1016/j.matdes.2014.10.076>.
 - [33] Wang Y, Shao WZ, Zhen L, Yang L, Zhang XM. Flow behavior and microstructures of superalloy 718 during high temperature deformation. *Mater Sci Eng -Struct Mater Prop Microstruct Process* 2008;497:479–86. <https://doi.org/10.1016/j.msea.2008.07.046>.
 - [34] Mirzadeh H, Najafizadeh A. Prediction of the critical conditions for initiation of dynamic recrystallization. *Mater Des* 2010;31:1174–9. <https://doi.org/10.1016/j.matdes.2009.09.038>.
 - [35] Poliak EI, Jonas JJ. A one-parameter approach to determining the critical conditions for the initiation of dynamic recrystallization. *Acta Mater* 1996;44:127–36. [https://doi.org/10.1016/1359-6454\(95\)00146-7](https://doi.org/10.1016/1359-6454(95)00146-7).
 - [36] Zeng Z, Chen L, Zhu F, Liu X. Dynamic recrystallization behavior of a heat-resistant martensitic stainless steel 403Nb during hot deformation. *J Mater Sci Technol* 2011;27:913–9. [https://doi.org/10.1016/S1005-0302\(11\)60164-3](https://doi.org/10.1016/S1005-0302(11)60164-3).
 - [37] Wang Y, Wang J, Dong J, Li A, Li Z, Xie G, et al. Hot deformation characteristics and hot working window of as-cast large-tonnage GH3535 superalloy ingot. *J Mater Sci Technol* 2018;34:2439–46. <https://doi.org/10.1016/j.jmst.2018.04.001>.
 - [38] Lu L, Hou L, Cui H, Huang J, Zhang Y, Zhang J. Hot deformation behavior and processing map of spray formed M3: 2 high speed steel. *J Iron Steel Res Int* 2016;23:501–8.
 - [39] Lin YC, Chen X-M. A critical review of experimental results and constitutive descriptions for metals and alloys in hot

- working. *Mater Des* 2011;32:1733–59. <https://doi.org/10.1016/j.matdes.2010.11.048>.
- [40] Cai Z, Ji H, Pei W, Tang X, Huang X, Liu J. Hot workability, constitutive model and processing map of 3Cr23Ni8Mn3N heat resistant steel. *Vacuum* 2019;165:324–36. <https://doi.org/10.1016/j.vacuum.2019.04.041>.
- [41] Bao S, Zhao G, Yu C, Chang Q, Ye C, Mao X. Recrystallization behavior of a Nb-microalloyed steel during hot compression. *Appl Math Model* 2011;35:3268–75. <https://doi.org/10.1016/j.apm.2011.01.024>.
- [42] Wei H, Liu G, Xiao X, Zhang M. Dynamic recrystallization behavior of a medium carbon vanadium microalloyed steel. *Mater Sci Eng - Struct Mater Prop Microstruct Process* 2013;573:215–21. <https://doi.org/10.1016/j.msea.2013.03.009>.
- [43] Zhang C, Zhang L, Shen W, Liu C, Xia Y, Li R. Study on constitutive modeling and processing maps for hot deformation of medium carbon Cr-Ni-Mo alloyed steel. *Mater Des* 2016;90:804–14. <https://doi.org/10.1016/j.matdes.2015.11.036>.
- [44] Han Y, Wu H, Zhang W, Zou D, Liu G, Qiao G. Constitutive equation and dynamic recrystallization behavior of as-cast 254SMO super-austenitic stainless steel. *Mater Des* 2015;69:230–40. <https://doi.org/10.1016/j.matdes.2014.12.049>.
- [45] Farnoush H, Momeni A, Dehghani K, Mohandesij A, Keshmiri H. Hot deformation characteristics of 2205 duplex stainless steel based on the behavior of constituent phases. *Mater Des* 2010;31:220–6. <https://doi.org/10.1016/j.matdes.2009.06.028>.
- [46] Wang W, Zhao J, Zhai RX, Ma R. Arrhenius-type constitutive model and dynamic recrystallization behavior of 20Cr2Ni4A alloy carburizing steel. *Steel Res Int* 2017;88:1600196. <https://doi.org/10.1002/srin.201600196>.
- [47] Zhao H, Qi J, Su R, Zhan H, Chen H, Bai L, et al. Hot deformation behaviour of 40CrNi steel and evaluation of different processing map construction methods. *J Mater Res Technol-Jmrt* 2020;9:2856–69. <https://doi.org/10.1016/j.jmrt.2020.01.020>.
- [48] Naghdy S, Akbarzadeh A. Characterization of dynamic recrystallization parameters for a low carbon resulfurized free-cutting steel. *Mater Des* 2014;53:910–4. <https://doi.org/10.1016/j.matdes.2013.07.031>.
- [49] Wei H, Liu G, Zhao H, Zhang M. Effect of carbon content on hot deformation behaviors of vanadium microalloyed steels. *Mater Sci Eng, A* 2014;596:112–20. <https://doi.org/10.1016/j.msea.2013.12.063>.
- [50] Zeng M, Cao J-C. Effect of Zr on dynamic recrystallization behavior of Ti-microalloyed low carbon steels. *Steel Res Int* 2020;91:2000104. <https://doi.org/10.1002/srin.202000104>.
- [51] Shaban M, Eghbali B. Characterization of austenite dynamic recrystallization under different Z parameters in a microalloyed steel. *J Mater Sci Technol* 2011;27:359–63. [https://doi.org/10.1016/S1005-0302\(11\)60074-1](https://doi.org/10.1016/S1005-0302(11)60074-1).
- [52] Wei H, Liu G, Zhao H, Kang R. Hot deformation behavior of two C-Mn-Si based and C-Mn-Al based microalloyed high-strength steels: a comparative study. *Mater Des* 2013;50:484–90. <https://doi.org/10.1016/j.matdes.2013.03.043>.
- [53] Zhao B, Zhao T, Li G, Lu Q. The kinetics of dynamic recrystallization of a low carbon vanadium-nitride microalloyed steel. *Mater Sci Eng, A* 2014;604:117–21. <https://doi.org/10.1016/j.msea.2014.03.019>.
- [54] Zhao H, Qi J, Liu G, Su R, Sun Z. A comparative study on hot deformation behaviours of low-carbon and medium-carbon vanadium microalloyed steels. *J Mater Res Technol* 2020;9:11319–31. <https://doi.org/10.1016/j.jmrt.2020.08.016>.
- [55] Badjena SK, Park JK. Effect of particles on the dynamic recrystallization behavior of Al-V-N micro-alloyed medium carbon steel. *Mater Sci Eng, A* 2012;548:126–33. <https://doi.org/10.1016/j.msea.2012.03.102>.
- [56] Han Y, Sun Y, Zhang W, Chen H. Hot deformation and processing window optimization of a 70MnSiCrMo carbide-free bainitic steel. *Materials* 2017;10:318. <https://doi.org/10.3390/ma10030318>.
- [57] Mirzadeh H, Cabrera JM, Prado JM, Najafizadeh A. Hot deformation behavior of a medium carbon microalloyed steel. *Mater Sci Eng, A* 2011;528:3876–82. <https://doi.org/10.1016/j.msea.2011.01.098>.
- [58] Yan T, Yu E, Zhao Y. Modeling of hot deformation behavior of 55SiMnMo medium-carbon steel. *J Iron Steel Res Int* 2013;20:125–30. [https://doi.org/10.1016/S1006-706X\(13\)60207-1](https://doi.org/10.1016/S1006-706X(13)60207-1).
- [59] Jafari M, Najafizadeh A. Correlation between Zener-Hollomon parameter and necklace DRX during hot deformation of 316 stainless steel. *Mater Sci Eng, A* 2009;501:16–25. <https://doi.org/10.1016/j.msea.2008.09.073>.
- [60] Momeni A, Dehghani K. Characterization of hot deformation behavior of 410 martensitic stainless steel using constitutive equations and processing maps. *Mater Sci Eng, A* 2010;527:5467–73. <https://doi.org/10.1016/j.msea.2010.05.079>.
- [61] Zhang W-F, Li X-L, Sha W, Yan W, Wang W, Shan Y-Y, et al. Hot deformation characteristics of a nitride strengthened martensitic heat resistant steel. *Mater Sci Eng, A* 2014;590:199–208. <https://doi.org/10.1016/j.msea.2013.10.020>.
- [62] Wenhui Z, Shuhua S, Deli Z, Baozhong W, Zhenhua W, Wantang F. Hot deformation behavior of a Nb-containing 316LN stainless steel. *Mater Des* 2011;32:4173–9. <https://doi.org/10.1016/j.matdes.2011.04.043>.
- [63] Momeni A, Abbasi M. Hot compression behavior of as-cast precipitation- hardening stainless steel. *J Iron Steel Res Int* 2007;14(5):66–70. [https://doi.org/10.1016/S1006-706X\(07\)60077-6](https://doi.org/10.1016/S1006-706X(07)60077-6).
- [64] Martins C de A, Poliak E, Godefroid LB, Fonstein N. Determining the conditions for dynamic recrystallization in hot deformation of C-Mn-V steels and the effects of Cr and Mo additions. *ISIJ Int* 2014;54:227–34. <https://doi.org/10.2355/isijinternational1.54.227>.
- [65] Beladi H, Hodgson PD. Effect of carbon content on the recrystallization kinetics of Nb-steels. *Scripta Mater* 2007;56:1059–62. <https://doi.org/10.1016/j.scriptamat.2007.02.029>.
- [66] Mejía I, Bedolla-Jacuinde A, Maldonado C, Cabrera JM. Determination of the critical conditions for the initiation of dynamic recrystallization in boron microalloyed steels. *Mater Sci Eng, A* 2011;528:4133–40. <https://doi.org/10.1016/j.msea.2011.01.102>.
- [67] López-Chipres E, Mejía I, Maldonado C, Bedolla-Jacuinde A, El-Wahabi M, Cabrera JM. Hot flow behavior of boron microalloyed steels. *Mater Sci Eng, A* 2008;480:49–55. <https://doi.org/10.1016/j.msea.2007.06.067>.
- [68] Kumar S, Aashranth B, Samantaray D, Davinci MA, Borah U, Bhaduri AK. Influence of nitrogen on kinetics of dynamic recrystallization in Fe-Cr-Ni-Mo steel. *Vacuum* 2018;156:20–9. <https://doi.org/10.1016/j.vacuum.2018.07.010>.
- [69] Gong B, Duan XW, Liu JS, Liu JJ. A physically based constitutive model of As-forged 34CrNiMo6 steel and processing maps for hot working. *Vacuum* 2018;155:345–57. <https://doi.org/10.1016/j.vacuum.2018.06.022>.

- [70] Zhou P, Ma Q-X. Dynamic recrystallization behavior and processing map development of 25CrMo4 mirror plate steel during hot deformation. *Acta Metall Sin-Engl Lett* 2017;30:907–20. <https://doi.org/10.1007/s40195-017-0613-4>.
- [71] Zahiri SH, Davies CHJ, Hodgson PD. A mechanical approach to quantify dynamic recrystallization in polycrystalline metals. *Scripta Mater* 2005;52:299–304. <https://doi.org/10.1016/j.scriptamat.2004.10.011>.
- [72] Nioi M, Pinna C, Celotto S, Swart E, Farrugia D, Husain Z, et al. Finite element modelling of surface defect evolution during hot rolling of Silicon steel. *J Mater Process Technol* 2019;268:181–91. <https://doi.org/10.1016/j.jmatprotec.2019.01.014>.
- [73] Duan XW, Liu JJ, Gong B, Li P, Liu JS. Experimental study and numerical simulation of dynamic recrystallization behavior of a high-strength steel. *Met Mater Int* 2021;27:1044–59. <https://doi.org/10.1007/s12540-019-00433-w>.
- [74] Wang S, Zhang M, Wu H, Yang B. Study on the dynamic recrystallization model and mechanism of nuclear grade 316LN austenitic stainless steel. *Mater Char* 2016;118:92–101. <https://doi.org/10.1016/j.matchar.2016.05.015>.
- [75] Huang X, Suzuki K, Watazu A, Shigematsu I, Saito N. Improvement of formability of Mg–Al–Zn alloy sheet at low temperatures using differential speed rolling. *J Alloys Compd* 2009;470:263–8. <https://doi.org/10.1016/j.jallcom.2008.02.029>.
- [76] Huang X, Suzuki K, Watazu A, Shigematsu I, Saito N. Microstructural and textural evolution of AZ31 magnesium alloy during differential speed rolling. *J Alloys Compd* 2009;479:726–31. <https://doi.org/10.1016/j.jallcom.2009.01.046>.
- Yan Peng*
Shuo Guo
Caiyi Liu
National Engineering Research Center for Equipment and Technology of Cold Strip Rolling, Yanshan University, Qinhuangdao, 066004, China
Silvia Barella
Department of Mechanical Engineering, Politecnico di Milano, Milan, 20156, Italy
Shicheng Liang
National Engineering Research Center for Equipment and Technology of Cold Strip Rolling, Yanshan University, Qinhuangdao, 066004, China
Andrea Gruttadauria
Carlo Mapelli
Department of Mechanical Engineering, Politecnico di Milano, Milan, 20156, Italy
- *Corresponding author.
E-mail address: pengyan@ysu.edu.cn (Y. Peng)
- 3 May 2022
Available online 11 July 2022
- <https://doi.org/10.1016/j.jmrt.2022.07.039>
2238-7854/© 2022 The Author(s). Published by Elsevier B.V. This is an open access article under the CC BY-NC-ND license (<http://creativecommons.org/licenses/by-nc-nd/4.0/>).